

Quantized many-body spin-valley textures in charge tunable monolayer MoS₂

J. Klein,^{1,2,*} A. Hötger,¹ M. Florian,³ A. Steinhoff,³ A. Delhomme,⁴ T. Taniguchi,⁵ K. Watanabe,⁵
F. Jahnke,³ A. W. Holleitner,¹ M. Potemski,⁴ C. Faugeras,⁴ J. J. Finley,^{1,†} and A. V. Stier^{1,‡}

¹Walter Schottky Institut and Physik Department,
Technische Universität München, Am Coulombwall 4, 85748 Garching, Germany

²Department of Materials Science and Engineering,
Massachusetts Institute of Technology, Cambridge, Massachusetts 02139, USA

³Institut für Theoretische Physik, Universität Bremen, P.O. Box 330 440, 28334 Bremen, Germany

⁴Université Grenoble Alpes, INSA Toulouse, Univ. Toulouse Paul Sabatier,
EMFL, CNRS, LNCMI, 38000 Grenoble, France.

⁵Research Center for Functional Materials, National Institute for Materials Science, 1-1 Namiki, Tsukuba 305-0044, Japan

(Dated: 2020-07-31)

We explore the many-body interaction of neutral, positively and negatively charged electron-hole pairs in a MoS₂ monolayer with the distinct spin and valley textures of resident charges via density dependent high field magneto-optical spectroscopy. For the neutral exciton we unexpectedly observe nonlinear valley Zeeman effects, which we explain by dipolar spin-interactions of the exciton with the spin and valley polarized Fermi sea. At electron densities below $4 \cdot 10^{12} \text{cm}^{-2}$ we observe quantum oscillations in the photoluminescence of the *intravalley* trion as well as a Landau level occupation dependent non-uniform Zeeman shifts from which we determine both effective electron and hole masses. By increasing the local charge density to a situation where the Fermi energy dominates over the other relevant energy scales in the system, the magneto-optical response becomes dependent on the occupation of the fully spin-polarized Landau levels in both K/K' valleys producing magneto-optical signatures of a many-body state. Our experiments unequivocally demonstrate that the exciton in monolayer semiconductors is a single particle boson only close to charge neutrality and that it smoothly transitions into a polaronic state with a spin-valley flavour that is defined by the local Landau level quantized spin and valley texture away from charge neutrality.

I. INTRODUCTION

A bosonic exciton immersed in a Fermi gas is an example of the *impurity-model* that can be understood in terms of a polaronic picture - dressing of the exciton by collective excitations of the many-body environment.¹⁻⁷ Such electron-electron interactions have been extensively studied in two-dimensional (2D) electron and hole gases like GaAs,⁸⁻¹⁰ AlAs^{11,12} and recently also in graphene,^{13,14} where typically the spin- and valley susceptibility of the system under investigation is enhanced. The strength of those effects depends on the extent of Coulomb interactions of the resident charges in such systems. Atomically thin quantum materials are well suited to experimentally study such phenomena since Coulomb interactions are inherently strong^{15,16} and the carrier density can be electrically controlled by gating.¹⁷⁻¹⁹ Therefore, 2D materials like the semiconducting transition metal dichalcogenide (TMDC) MoS₂ and their heterostructures represent an ideal material platform for exploring and controlling interaction enhanced collective phenomena, such as magnetism²⁰ and many-body related phases in condensed matter.²¹⁻²³ Crucially, robust optical selection rules provide access to spin and valley degrees of freedom^{24,25} opening the way to study the magnetic properties of such polarons.

The magnetic field dependence of fundamental optical excitations in 2D TMDCs encode the evolution of the total magnetic energy. This includes the carrier spin, the valley magnetic moment (Berry phase) and cyclotron

phenomena arising from quantization of electrons and/or holes into discrete Landau levels (LLs).²⁶⁻³³ However, even the simplest and most fundamental Coulomb bound quasi-particle, a single neutral exciton, is susceptible to Coulomb interactions with surrounding excess carriers to form an exciton-polaron.^{1,6,7} The transition from a non-interacting exciton into an exciton-polaron is not abrupt, but rather occurs gradually as the carrier density is increased. As such, the 2D nature of monolayer TMDCs and the ability to form gated heterostructures allows to inject excess carriers from the intrinsic regime up to the Mott transition³⁴ ($n \sim 10^{13} \text{cm}^{-2}$) to study correlated phenomena that arise from many-body interactions of excitons with the underlying Fermi sea.^{6,7,35,36} Sampling this transition via quantum transport studies is intrinsically restricted to the high density regime where LLs with high filling factors are probed.^{19,37-42} In contrast, optical measurements facilitate access to the entire density regime, for positive and negative excess carrier densities.^{31,32} Specifically in the low density regime, valley dichroism in the presence of a magnetic field generates a unique local spin and valley texture of excess carriers which so far has not been accounted for theoretically or studied experimentally. Here only a few spin-polarized LLs with low filling factors are involved that are expected to have a significant impact on the many-body environment, and therefore the interaction with excitons (Fermi-polarons). This further highlights the necessity for careful density control when studying the spin-valley physics of 2D materials.

II. CARRIER CONCENTRATION DEPENDENT MAGNETO-PL

In this manuscript, we apply magneto-optical methods to investigate the spin and valley susceptibility of monolayer MoS₂ in dual gated devices (see Fig. 1b). Hereby, we explore the magneto optical response throughout the phase space ranging from a virtually absent local carrier density to a situation where the Fermi energy (E_F) dominates over the spin-, exchange- and cyclotron-energies.

III. QUANTIZED SPIN-VALLEY TEXTURE

Figure 1a schematically depicts the spin and valley band sequence of monolayer MoS₂ in an excitonic picture. Electron-hole exchange leads to an optically dark alignment of the spin-orbit split conduction bands c_1 and c_2 , which has been theoretically proposed⁴³ and recently verified experimentally.^{37,44} The dark-bright exciton energy splitting is $\Delta_{db} = 14$ meV.^{37,44} Throughout this manuscript, we describe all observed effects on the basis of this interacting excitonic picture.

For zero magnetic field and a gate potential for which E_F is situated slightly above the lower conduction band minima (c_1), an equal number of spin-up (\uparrow) and spin-down (\downarrow) electrons occupy the bands at K and K' ($N_\uparrow = N_\downarrow$) resulting in zero net spin polarization interacting with the exciton (Fig. 1a). However, an applied magnetic field breaks time-reversal symmetry, shifts the conduction band minima, and the resident electrons condense into LLs resulting in an imbalance between the occupation of the K and K' valleys. A direct consequence is the emergence of a spin-polarized Fermi sea ($N_\uparrow \neq N_\downarrow$) in either K or K' (depicted schematically for K' in Fig. 1c) for positive and negative magnetic fields. The resulting spin-valley texture experienced by the exciton depends on the carrier concentration (Fermi level position) and the direction and magnitude of the applied magnetic field. This is visualized in the calculation of the spin-valley texture of monolayer MoS₂ in Fig. 1d. Here, the global degree of spin polarization $\eta_s = (N_\uparrow - N_\downarrow)/(N_\uparrow + N_\downarrow)$ enters different regimes ranging from unity spin polarization at low carrier concentration and high magnetic fields (regime II), through intermediate densities where both spin- \uparrow and spin- \downarrow valley textures exist (regime III) to the absence of spin polarization at highest densities where the Fermi level resides well above the minimum of the upper conduction band c_2 (regime IV). This quantized spin and valley texture is the result of the magnetic field dependent degeneracy of fully spin polarized Landau levels in 2D TMDCs. For our consideration, we model only the relevant LLs in the conduction bands with a finite inhomogeneous broadening (4 meV) and determine the number of spin- \uparrow and spin- \downarrow electrons from integrating over the corresponding density of states (see Fig. 1e and further details in the Supplemental Material).

Our experiment is designed to excite the sample with

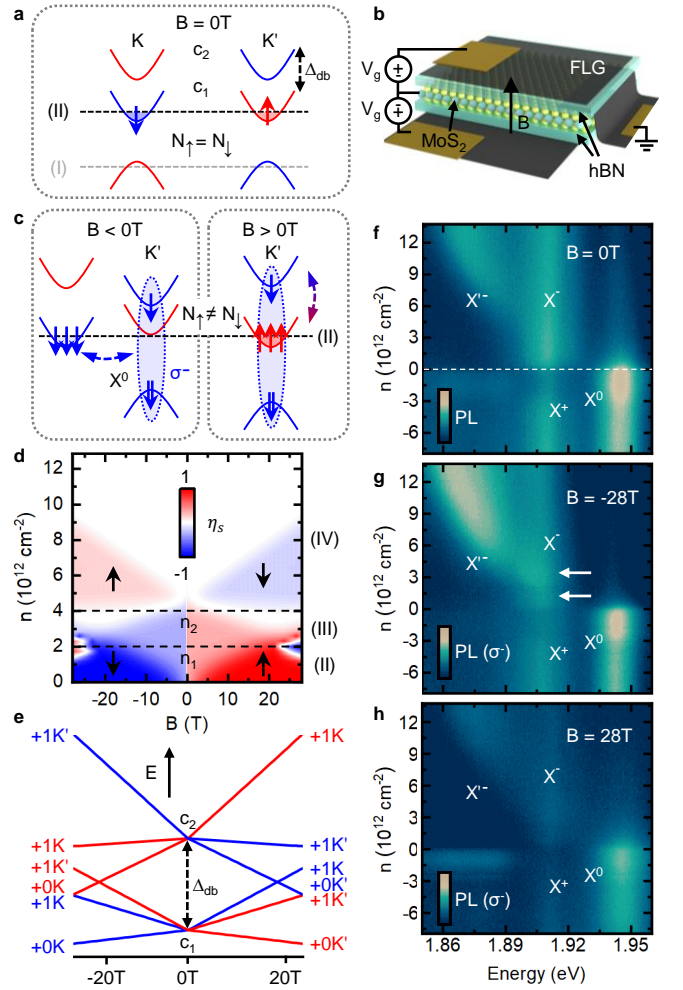


Fig. 1. **a**, Spin and valley exciton band structure at the K and K' points of monolayer MoS₂ for restored time-reversal symmetry ($B = 0$ T). For low electron charging ($n < n_1$) in regime II, E_F situated in c_1 , the number of spin up N_\uparrow and spin down N_\downarrow electrons is equal. Electron spins are ordered anti-parallel. **b**, Schematic of the dual-gate monolayer MoS₂ vdW device in Faraday geometry. A monolayer MoS₂ is sandwiched between hexagonal boron nitride (hBN) and contacted with thin graphite (FLG) electrodes. **c**, A finite magnetic field ($B \neq 0$ T) breaks time-reversal symmetry inducing an electron spin imbalance ($N_\uparrow \neq N_\downarrow$) that results in a paramagnetic out-of-plane spin ordering, and therefore an overall net magnetization in the lower spin-split conduction band c_1 in regime II interacting with the X^0 . For positive magnetic field, this interaction is of *intravalley*-type, while for negative magnetic field of *intervalley*-type. **d**, Calculated degree of spin polarization η_s (see Supplemental Material for further details) showing the density and magnetic field dependent spin and valley texture in the conduction bands. **e**, Corresponding calculated LL fan diagram (see Supplemental Material for further details). **f-h**, Gate-voltage controlled low-temperature ($T = 5$ K) μ -PL in the electron and hole charged regime at $B = 0$ T, $B = -28$ T and $B = 28$ T. The dashed lines shows the point of charge neutrality ($n \sim 0$ cm⁻²). Arrows for $B = -28$ T highlight LLs in X^- .

unpolarized light and detect σ^- -PL at $T = 5$ K. Due to the robust optical selection rules in monolayer TMDCs we therefore only probe the emission from excitonic recombination in the K' valley for positive and negative B .²⁴ As such, our magneto optical data contains direct information of η_s -dependent effects on the emission. Figures 1f-h compare false colour images of the PL spectra recorded at $B = 0$ T, $B = -28$ T and $B = 28$ T as a function of carrier concentration. We symmetrically apply a voltage to the top and bottom gates, which effectively counteracts Fermi-level pinning due to the reduction of band tail states.^{45,46} This allows us to access the p-charged regime for the first time in MoS₂. The data reveal near Lorentzian shaped lines due to the hBN encapsulation of the monolayer semiconductor.⁴⁷⁻⁴⁹ The zero field spectra show the neutral exciton X^0 at 1.944 eV at charge neutrality, which is quickly quenched at moderate densities of $n_1 \geq 2 \cdot 10^{12} \text{cm}^{-2}$. The intravalley charged exciton X^- at ~ 1.91 eV (discussed in detail below) is visible at low to moderate carrier density. Another PL feature, labelled X'^- in Fig. 1f, appears red shifted from X^- at $n_2 \sim 4 \cdot 10^{12} \text{cm}^{-2}$ and quickly gains intensity to dominate the spectrum at higher carrier densities. In addition to the well-known features in the electron charged regime, we also observe the positive trion, X^+ in the hole charging regime I. The feature appears at virtually the same energy as the X^- . We repeated the measurement for various static magnetic fields ranging from -28 T to 28 T (all data presented in the Supplemental Material also for a second device). Figures 2a and 2b show the magnetic field dependent X^0 PL close to charge neutrality ($n \sim 0 \text{cm}^{-2}$) and for low electron densities ($n \sim 1.45 \cdot 10^{12} \text{cm}^{-2}$). Strikingly, while the valley Zeeman shift is completely linear at charge neutrality, it becomes nonlinear with electron doping. This is summarized in Fig. 2c, where the B -field dependent peak positions for a sequence of charge doping are shown. Clearly, the valley Zeeman shift remains linear throughout the hole charging regime and becomes increasingly nonlinear upon moving into the electron charging regime. This behaviour is a direct consequence of the interaction of the exciton with the local spin-polarized Fermi-texture.

An applied magnetic field, which breaks time reversal symmetry, lifts the K/K' valley degeneracy by shifting time-reversed pairs of states in opposite energetic directions in accord with the Zeeman energy $-\mu_B \cdot B$.²⁵ This effect will shift the exciton energy in the situation when the magnetic moment of conduction and valence bands are not equal, $\Delta E_{VZ} = -(\mu^c - \mu^v) \cdot B = \frac{1}{2}g\mu_B B$. In general, the total magnetic moment is made up of an orbital and a spin component $\mu = \mu^{orb} + \mu^s$, where $\mu^{orb} = -\frac{e}{2m_e}l_z$ and $\mu^s = \frac{eg_e}{2m_e}s_z$. Due to the hybridization of the $d_{x^2-y^2}$ and d_{xy} orbitals in the valence band, the Bloch electrons at K/K' provide an angular momentum of $l_z = \pm 2\hbar$ such that an estimate for the valley Zeeman splitting in a simple, non-interacting model is $\mu = -4\mu_B$.²⁷ Indeed, for most semiconducting monolayer TMDCs close to charge neutrality, linear valley Zeeman

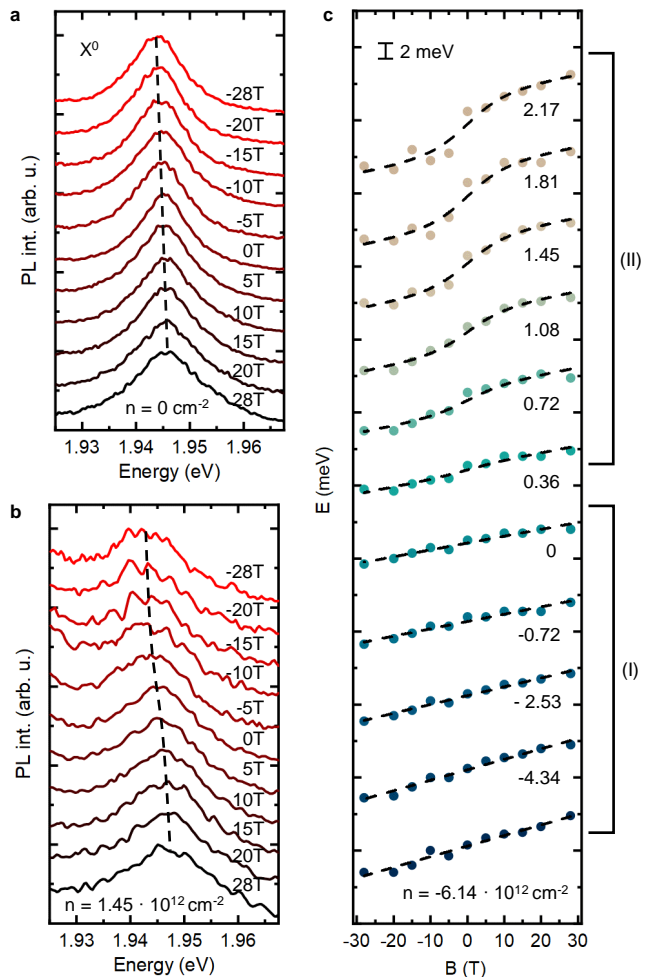


Fig. 2. **a**, and **b**, Normalized μ -PL spectra of X^0 for applied magnetic fields at $n = 0 \text{cm}^{-2}$ ($n = 1.45 \cdot 10^{12} \text{cm}^{-2}$) from -28 T to 28 T. The solid lines are guide to the eye. **c**, Carrier density dependent valley Zeeman shift of the X^0 in the electron and hole charged regime. The valley Zeeman shift in the hole charged regime I is linear and increases continuously at higher hole density. The minimum g -factor is obtained at $n = 0 \text{cm}^{-2}$ with -1.27 ± 0.09 . For electron charging, regime II, the Zeeman shift undergoes a strong nonlinearity which is fit with Eq. 2. The nonlinearity increases monotonously for densities ($n < n_1 \sim 2 \cdot 10^{12} \text{cm}^{-2}$).

splitting for neutral excitons with g -factors near $g \sim -4$ are reported.^{16,26-29,50-52} Such g -factors are reproduced well by recent first-principle studies including excitonic effects.⁵³ However, as pointed out in Ref.⁵⁰ and demonstrated in the Supplemental Material, the decomposition of orbital magnetic moments into a contribution due to *inter*-cellular hopping, captured by a lattice model, and atom-like *intra*-cellular corrections is a delicate problem. In a simple two-band model, the structure of the lattice term leads to equal *inter*-cellular contributions for conduction and valence electrons. Breaking of the electron-hole symmetry is expected due to transitions from each

band, respectively, to energetically higher and lower lying bands. Moreover, if the two fundamental bands are composed of localized orbitals that do not allow for atom-like dipole transitions (e.g. d_{z^2} - and $d_{x^2-y^2}/d_{xy}$ -orbitals as in MoS₂), the *intra*-cellular corrections will vanish. The orbital exciton g -factor will therefore be zero in a two-band model. This is consistent with the $\mathbf{k} \cdot \mathbf{p}$ -picture discussed in Ref.⁵⁰. At charge neutrality, we measure a valley Zeeman g -factor of the neutral exciton, $g_{X^0} = -1.27 \pm 0.09$. This value is consistent with recent reports of the valley Zeeman splitting in high quality and hBN encapsulated MoS₂^{48,54} and contrasts with earlier work on non-encapsulated monolayer MoS₂ samples.^{51,55} Our measured g -factor appears to be unusually small compared to the valley Zeeman splitting for excitons in other TMDC materials, however, the simple estimate described above and even the most sophisticated theoretical approaches to date ignore the many-body nature of the electron-hole pair which we demonstrate in the remainder of this manuscript. This is therefore an indication that specifically for monolayer MoS₂, but also for other 2D materials,⁵⁶ the non-interacting model might not be sufficient to fully capture the exciton spin physics. We further note that the exciton g -factor results from couplings of energetically remote bands,⁵⁷ which may be perturbed by free carriers as well as impurities.⁴⁶

The nonlinear valley Zeeman shift of the exciton emerging in the electron charged regime II shown in Fig. 1d results from a dipolar spin-interaction of X^0 with the spin-polarized Fermi sea since the lowest LL for all magnetic fields is spin- \uparrow polarized (see Fig. 1e). Similar physics can be found for electrons interacting with local magnetic moments in dilute magnetic semiconductors⁵⁸ or proximity effects between a ferromagnetic substrate and excitons in a monolayer semiconductor.^{59,60} In our case, the effective magnetic moment originates from a magnetic field induced net spin polarization of excess carriers as depicted schematically in Fig 1c. Qualitatively, this can be pictured as a paramagnetic spin ordering effect of conduction band electrons where the MoS₂ effectively undergoes a *ferrimagnetic-to-ferromagnetic* phase transition.⁴² When a sufficiently large magnetic field is applied, the valley degeneracy is lifted, which leads to a re-population of electrons into the lowest conduction band LL, and therefore a net spin imbalance, $S_Z(B) = -1/2 \cdot B_J(x)$, between the valleys occurs. Here, the Brillouin function is⁵⁸

$$B_J(x) = \frac{2s_z + 1}{2s_z} \coth\left(\frac{2s_z + 1}{2s_z}x\right) - \frac{1}{2s_z} \coth\left(\frac{1}{2s_z}x\right) \quad (1)$$

where $s_z = 1/2$ is the electron spin in the lower c_1 conduction band and $x = g\mu_B s_z B/k_B T$. The net magnetization is then $M \sim \Delta N \cdot S_Z(B)$ with the total number of polarized electron spins $\Delta N = |N_\downarrow - N_\uparrow|$. Therefore, the total valley Zeeman g -factor for the exciton in regime II can be expressed as the addition of spin and valley net magnetization effects as

$$g^*(n, B) = g_{X^0} + g_m(n) \cdot S_Z(B) \quad (2)$$

such that the nonlinear valley Zeeman shift is $\Delta E_{VZ}^{X^0}(n, B) = 1/2 g^*(n, B) \mu_B B$. As shown by the fits to the data in Fig. 2c, this simple model captures the nonlinear valley Zeeman shift surprisingly well. Most strikingly, we find that g^* monotonically increases from the value at charge neutrality to the trion g -factor (see Fig. 5a), showing the direct dependence of the exciton g -factor on the carrier density and strongly pointing towards the exciton having the character of a spin-polarized magnetic polaron at finite electron density.

IV. TRION FINE STRUCTURE IN MONOLAYER MoS₂

When the electron density is increased further, the oscillator strength shifts away from X^0 due to the formation of negatively charged excitons (attractive polarons³⁵). Owing to the optically dark alignment of the conduction bands in the exciton picture of monolayer MoS₂,^{37,43,44} we expect a singlet-triplet trion fine structure, similar to observations for WSe₂ and WS₂.⁶¹⁻⁶⁵ Recent experimental work reported first indications for singlet and triplet trions.⁵⁴ We further extend this picture with our data on the gate-tunable trion fine structure in combination with first-principle calculations that include electron-hole exchange interaction. Figure 3a illustrates three trion configurations: an *intravalley* singlet $T_{K\uparrow K\downarrow K\uparrow}^{eeh}$ and an *intervalley* triplet trion $T_{K'\downarrow K\downarrow K'\downarrow}^{eeh}$ whose binding energy differs due to electron-hole exchange interaction U_{eh} as well as an *intervalley* singlet trion $T_{K'\downarrow K\uparrow K'\downarrow}^{eeh}$ where both electrons are located in the upper conduction bands c_2 . We numerically solve a generalized three-particle Schrödinger equation to determine resonances in the optical absorption of hBN encapsulated monolayer MoS₂ at low carrier concentration. The method is combined with material-realistic band structures and bare as well as screened Coulomb matrix elements on a G_0W_0 level (see Supplemental Material). Results for the calculated optical absorption in Fig. 3c reveal the three trion contributions T_1 , T_2 and T_3 as individual peaks. Their experimental counterparts can be identified in Fig. 3b, where it is also shown that the corresponding oscillator strength progressively increases with electron density. From our calculations, we can directly distinguish between wave function contributions of the expected trion configurations (see Fig. 3d). Most importantly, we find that the lowest energy trion, T_1 , is predominantly the singlet *intravalley* trion while T_2 and T_3 are singlet and triplet *intervalley* trions. The absolute and relative energies of T_1 , T_2 and T_3 are in very good agreement with our experimental data, supporting our identification. Note that the binding energies of singlet *intravalley* trion and Coulomb exchange split *intervalley* triplet trion strongly depend on the ratio of the electron

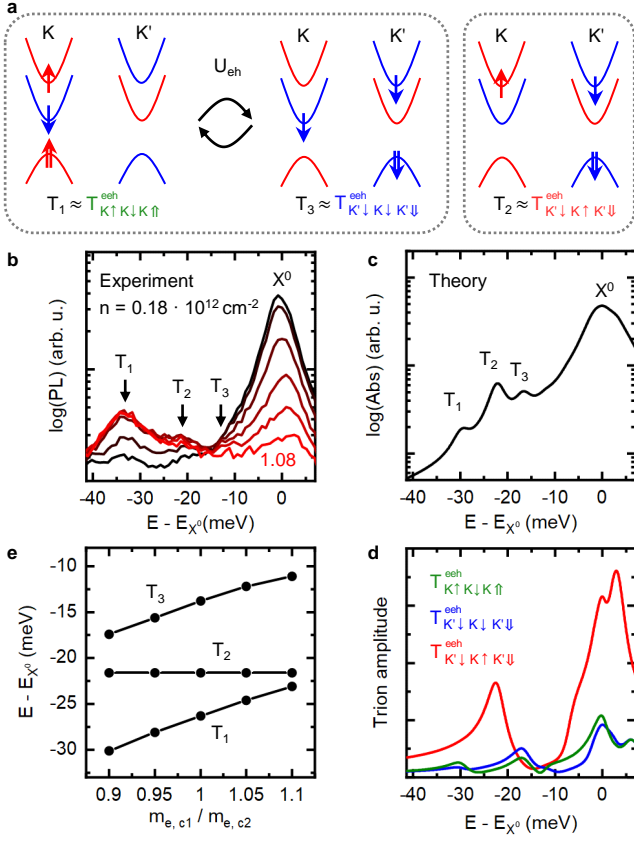


Fig. 3. **a**, Trion fine structure in monolayer MoS₂: *Intravalley* singlet $T_{K\uparrow K\downarrow K\uparrow}^{eeh}$ (left) and *intervalley* triplet trion $T_{K'\downarrow K\downarrow K'\downarrow}^{eeh}$ (center) from electron-hole exchange interaction U_{eh} and *intervalley* singlet trion $T_{K'\downarrow K\uparrow K'\downarrow}^{eeh}$ (right). **b**, Logarithmic plot of the experimental trion fine structure T_1 , T_2 and T_3 from PL for electron concentrations ranging from $n = 0.18 \cdot 10^{12} \text{cm}^{-2}$ (black) to $n = 1.08 \cdot 10^{12} \text{cm}^{-2}$ (red) from device *B*. **c**, Calculated absorption spectrum of hBN encapsulated monolayer MoS₂ for a carrier density of $n = 0.1 \cdot 10^{12} \text{cm}^{-2}$ revealing the same trion fine structure. A phenomenological homogeneous broadening of 2 meV (HWHM) has been used. **d**, Corresponding wave function contributions of the trion configurations to the absorption spectrum of hBN encapsulated monolayer MoS₂. **e**, Binding energies of trions T_1 , T_2 and T_3 as a function of the ratio between effective electron mass of upper and lower conduction band. Results are obtained using an effective mass model for the band structure around the K/K' points of the two lowest conduction (highest valence) bands.

masses in c_1 and c_2 (see Fig. 3e). Throughout the remainder of the manuscript we label the most prominent *intravalley* singlet trion T_1 as the "negative trion" X^- .

V. INTRAVALLEY TRION QUANTUM OSCILLATIONS

We now continue to explore interactions of the Fermi sea with X^- and X^+ in our devices and, specifically, their magneto-optical properties. The interaction strength with the Fermi sea in 2D electronic systems is conventionally parameterised by the dimensionless Wigner-Seitz parameter $r_S = 1/(\sqrt{n\pi}a_B)$.⁶⁶ Here, the X^0 (X^-) Bohr radius of hBN encapsulated MoS₂ is $a_B = 1.3 \text{ nm}$ ⁵² ($a_B = 2.1 \text{ nm}$).⁶ In our experiment ($n_{max} \sim 14 \cdot 10^{12} \text{cm}^{-2}$), we therefore predict that $1.2 < r_S < \infty$, illustrating that interactions ranging from strong to weak can be explored. Figure 4a shows a typical example of the X^- PL recorded at $B = -28 \text{ T}$ as a function of carrier density. The X^- integrated PL intensity, as shown in Fig. 4b, exhibits weak quantum oscillations marked with arrows. The peaks of these quantum oscillations are attributed to half filling of LLs with filling factors $\nu = +0$ and $\nu = +1$.³² As detailed in the Supplemental Material and plotted in Fig. 4c, the position of the peaks marked by arrows shift linearly with B . We conclude that X^- decays into a photon and an electron in a fully spin-and valley polarized Landau level (see Fig. 4e).^{30,32,67} As shown in the PL intensity map Fig. 4a, increasing the density above $n_2 \sim 4 \cdot 10^{12} \text{cm}^{-2}$ simultaneously quenches the 1st LL and the optical feature X'^- appears $\sim 18 \text{ meV}$ below X^- . The density n_2 is significant, since it corresponds to the point where E_F enters into the upper conduction bands c_2 in the interaction picture (regime IV).³⁷ Linking the electron density to the known energy splitting of the conduction bands (Δ_{db}),⁴⁴ we deduce an electron effective mass of $(0.44 \pm 0.15)m_e$ from the linear-in- B shift of the LLs (see details in Supplemental Material). This value is in excellent agreement with theory⁶⁸ but is smaller than that deduced from recent transport experiments,³⁷ most likely since transport samples a larger region of the Brillouin zone and carriers may also reside in the Σ valleys, which have a larger mass.⁶⁹ The density dependent valley Zeeman shifts of the X^- are presented in Fig. 4d. When the electron density is so low such that only the $\nu = +0$ LL is occupied in c_1 , the valley Zeeman shift for positive and negative magnetic fields are equal. However, for densities where the $\nu = +1$ LL is occupied (n_1), a strong asymmetry emerges in positive and negative magnetic fields. A quantitative description of the trion valley Zeeman shift at fixed density has recently been reported for singlet and triplet trions in WSe₂⁷⁰ which applies very well to our situation for MoS₂. In the case of X^- recombination, the final state is an electron in a LL.⁷⁰ Therefore, the observed valley Zeeman splitting of the X^- , $\Delta E_{VZ}^{X^-}(n, B) = 1/2(\tau_z g_{X^-} - \tau_e g_e)\mu_B B - g_l(n)\mu_B |B|$, is sensitive to the density dependent LL occupation, $g_l(n)$. For a density above $n_1 \sim 3 \cdot 10^{12} \text{cm}^{-2}$, the combination of spin, valley and cyclotron energy results in asymmetric LL dispersions in positive and negative magnetic fields for LLs with filling factors $\nu \geq +1$. As shown in Fig. 4e, this manifests itself as asymmetric slopes for positive and

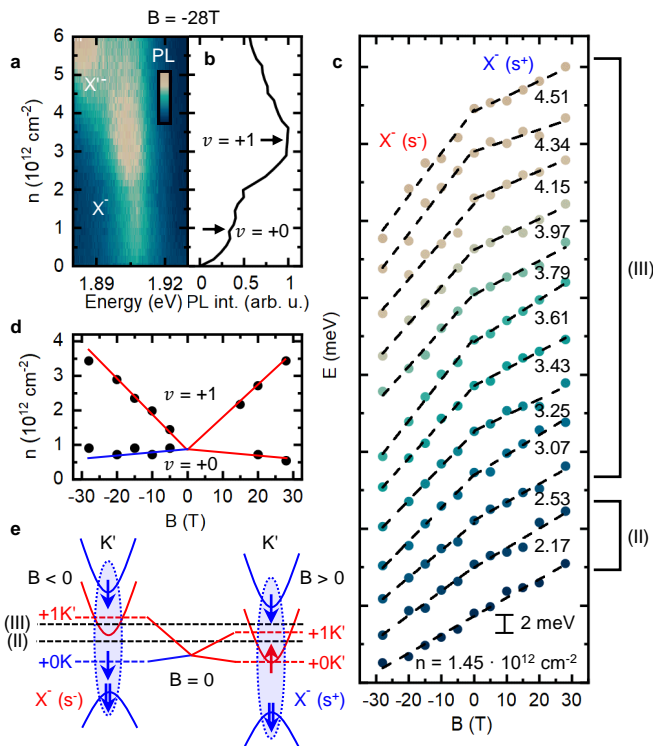


Fig. 4. **a**, Electron density dependent μ -PL of the X^- and onset of X'^- at $B = -28$ T. **b**, Corresponding integrated X^- intensity. The X^- reveals LL quantization as indicated by the dashed lines with filling factor $\nu = +0$ and $\nu = +1$. **c**, Corresponding LL fan diagram from which an electron mass of $0.44 \pm 0.15m_e$ is deduced. Solid lines serve as a guide to the eye. **d**, X^- valley Zeeman shift. The effective g -factor for negative magnetic field increases due to LL population effects. **e**, Band configuration including the relevant LLs in the lower conduction band of the *intravalley* trion singlet X^- for negative (s^-) and positive (s^+) magnetic field. Regime II: Only the LL with filling factor $\nu = +0$ is filled in the K (K') valley for negative (positive) magnetic field. Regime III: For negative field LL $\nu = +0$ is populated in K while $\nu = +0$ and $\nu = +1$ are in K' for positive magnetic fields. Regime IV is reached when the upper conduction bands c_2 are populated corresponding to an electron concentration of $n = 4 \cdot 10^{12} \text{cm}^{-2}$.

negative field directions as the trion energy depends on the final state (electron in a LL). We obtain the hole mass $(0.69 \pm 0.15)m_h$ from the average of the X^- g -factor in positive and negative field directions and by using the electron mass determined above (for details see Supplemental Material). By analyzing the data shown in Fig. 4 we obtain a constant mass in the regime where the overall spin texture in the system is negligible (see Fig. 1d and Supplemental Material). This suggests that the hole mass is indeed constant and enhancements of the spin-valley susceptibility are predominantly spin-driven, similar to observations in previous works.¹⁹

VI. MANY-BODY INTERACTION EFFECTS WITH EXCITONS AND MAGNETIC SUSCEPTIBILITY

We now summarize the valley susceptibility of all features in our accessible density range in Fig. 5a and provide a unified picture of the magnetic response of neutral and charged excitons in a many-body spin and valley environment. For the X^0 , we observe a monotonous increase of the g -factor from -1.27 at charge neutrality to -2.1 at the highest hole density (regime I). In this regime, the X^+ g -factor tracks the g -factor of X^0 with a value of $-(3.52 \pm 0.35)$. This observation suggests that the extra hole adds $\sim 1.5\mu_B$ to the valley susceptibility of the exciton. Upon introduction of electrons to the system and using Eq. 2 to obtain $g^*(n, B = 28 \text{ T})$, the magnetic moment of X^0 (see Fig. 2c) increases monotonically with carrier concentration, starting at charge neutrality and peaking at $g^* \sim -5.5$ for a density of $n_1 \sim 2 \cdot 10^{12} \text{cm}^{-2}$. This suggests that for $n < n_1$, the increased magnetic susceptibility of X^0 arises from the spin-polarized Fermi sea in the lower K' valley (see Fig. 1d and e) and the magnitude of $g^*(n, B)$ is highly sensitive to the local electron concentration. This conclusion may explain the large variation of reported g -factors for excitons in MoS₂ in the literature,^{48,51,52,54,55} highlighting the importance for studying valley Zeeman shifts with controlled excess carrier densities in MoS₂ and all other TMDCs. Crucially, $g^*(n, B)$ smoothly approaches the g -factor observed for X^- at higher electron concentrations, indicating that both states have a similar spin and valley structure. This finding indicates that the spin-polarized electrons interact with X^0 in a manner such that the strength is directly proportional to the number of gate-induced electrons. In other words, X^0 interacts with the spin-polarized Fermi sea (see Fig. 5b) while the strength of the interaction is tuned by the Fermi energy, very similar to the Kondo problem of an isolated impurity spin interacting with a spin-polarized Fermi sea.⁷¹ For high densities, the spin structure of X^0 increasingly resembles that of X^- . Indeed, at the carrier density of n_1 , X^0 sees on average ~ 0.1 electrons within its wave function - a diameter of $2a_B$. Hence, tuning both carrier density and magnetic field may open up routes to probe the strength of the interaction between X^0 and the spin-polarized Fermi sea.

For the X^- in the moderately electron charged regime II with densities from $0 < n < n_1$ we determine a g -factor of ~ -3 suggesting that the magnetic moment of X^- and X^+ , are qualitatively similar. Indeed, both charged excitons are singlets where the final state $|f\rangle$ is a free carrier in the 0^{th} LL. The only difference is that the X^+ is an *intervalley* particle while for the X^- , the configuration is of the *intravalley* type. Raising the electron concentration from moderate (n_1) to high (n_2) electron densities ($r_S \sim 3.1 - 2.2$), we find an asymmetry of the valley Zeeman shift. We attribute this increase to LL occupation differences in K and K' valley due to the lifting of the

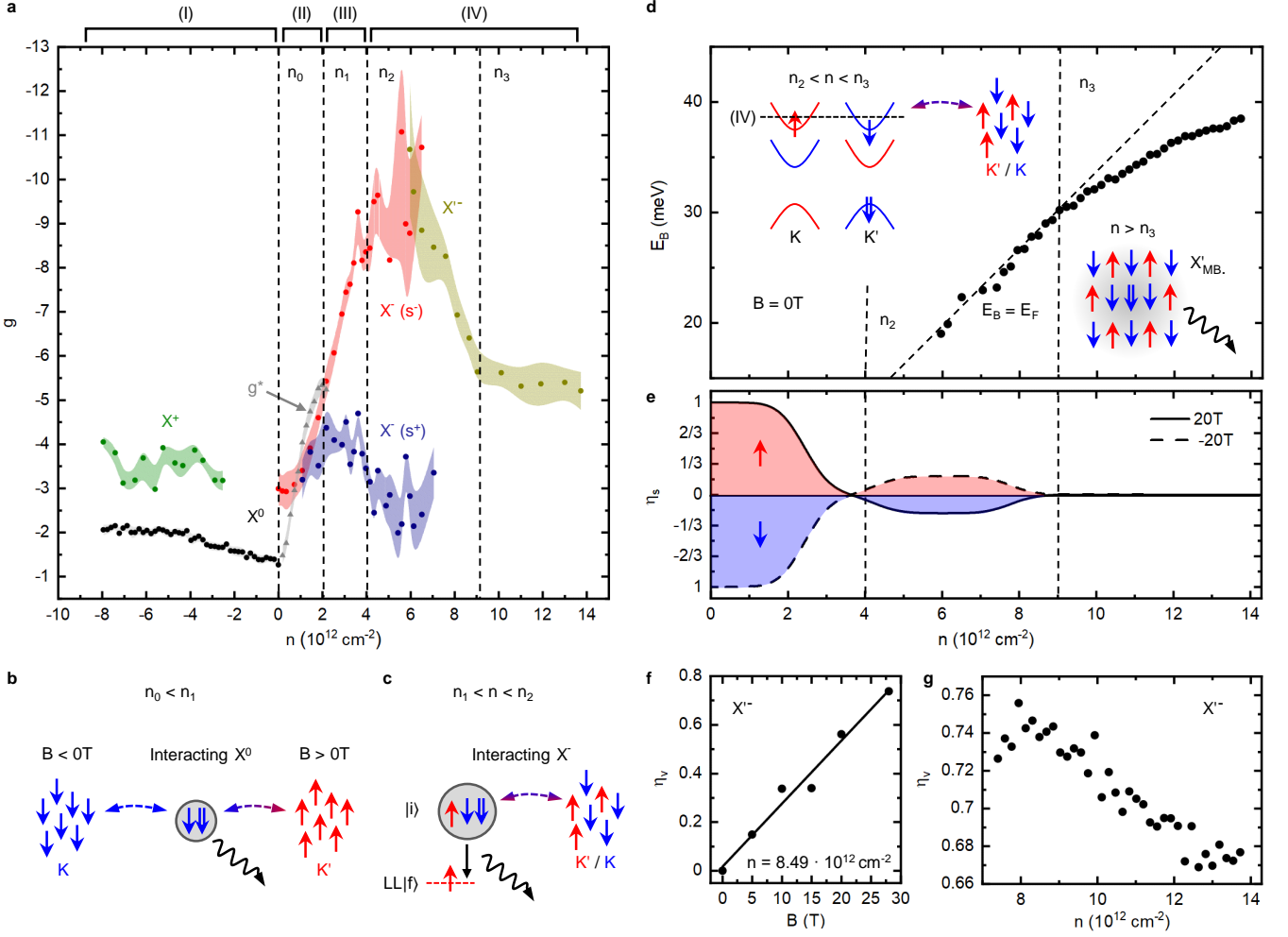


Fig. 5. **a**, Carrier density dependent g -factors of the neutral exciton X^0 (black and gray data), the negatively (red and blue data) and positively (green data) charged excitons X^- and X^+ , and the X'^- feature (yellow data). Regime I: Linear increase of X^0 g -factor and constant g -factor of X^+ within the error. Regime II: Linear increase of effective X^0 g -factor $g^* = g(n=0) + g_m$ with g_m obtained from Brillouin function fits (see Fig. 2h). Regime III: Non-uniform g -factor of the *intravalley* singlet trion X^- for negative and positive magnetic fields for moderate carrier densities $n_1 < n < n_2$. Regime IV: For the highest carrier densities $n \gg n_2$ the X'^- reveals a decreasing g -factor. **b**, Schematic sketch of many-body interaction of exciton and spin-polarized Fermi sea. The X^0 maintains most of its bosonic character at moderate carrier concentrations (regime II) but is gradually dressed by the spin-polarized electron bath at the K/K' valley. Thus, emission resembles an interacting X^0 (Magnetic Fermipolaron). **c**, Regime III: the X^0 is strongly dressed from the electron bath forming a negatively charged exciton X^- . This X^- interacts with a weakly-polarized electron bath, since the Fermi-level is now also populating the K valley. The emission reflects an interacting X^- as initial state $|i\rangle$ with an electron in a spin polarized LL as the final state $|f\rangle$. **d**, Carrier density dependence of the X'^- binding energy E_B . For $n_2 < n < n_3$ E_B is linear with E_F while it becomes sub-linear for $n > n_3$. For the highest carrier densities (regime IV), the quasi-particle excitation is strongly interacting and dissolving into a many-body state X'_{MB} . **e**, Electron concentration dependence of the degree of global spin polarization η_s for $B = -20$ T and 20 T. **f**, Magnetic field dependence of the degree of valley polarization η_v of the X'^- for $n = 8.49 \cdot 10^{12} \text{ cm}^{-2}$. Solid line is a linear fit to the data. **g**, Electron concentration dependence of η_v at $|B| = 28$ T.

time-reversal symmetry in the lower conduction bands c_1 . This is supported by the observation of LL intensity oscillations ($\nu = +0, +1$) in the *intravalley* X^- emission (see Fig. 4). While the g -factor at positive magnetic field remains constant within the error, the magnitude of Zeeman shift at negative magnetic fields, and therefore

the g -factor increases to ~ -10 . Similar to X^0 , X^- also interacts with electrons in the Fermi sea. However, unlike for X^0 the local spin valley texture admits electrons residing in both K and K' valleys since E_F is located in both lower conduction bands (regime III). This picture is also supported by the spin texture, shown in Fig. 5e and

reflected by the degree of circular polarization of emission. Here, $\eta_s < \pm 0.3$ for 20 T (and -20 T) reflecting the presence of both spin- \uparrow and spin- \downarrow electrons around X^0 . While the exciton on average interacts with less than one electron in regime II, the average number of electrons seen by the trion in regime III increases from $\sim 0.3e^-$ to $\sim 0.6e^-$.

At higher concentrations ($n > n_2$) (regime IV), the emission is quickly dominated by the feature X'^- , while the *intravalley* X^- emission quenches. The shift of spectral weight from the X^- to X'^- was found to depend on sample quality and generally occurred quicker for cleaner samples with less disorder. In all samples, the X'^- emission emerges precisely at the carrier density when E_F shifts into the upper conduction bands c_2 ($n_2 \sim 4 \cdot 10^{12} \text{cm}^{-2}$ in our devices).³⁷ This feature has recently been attributed to a Mahan-like exciton,⁷² which is a stable bound state at high carrier concentration,⁷³ in the context of a spontaneous magnetic phase transition in monolayer MoS₂ or an exciton-plasmon-like excitation,⁷⁴ but it is not yet fully understood. We find that the valley Zeeman shift of this feature is symmetric and linear in magnetic field for all accessible densities (see Supplemental Material). The g -factor of X'^- is equal to $g_{X^-(s^-)}$ at n_2 , which suggests a qualitatively similar magnetic moment as the X^- in negative magnetic field. Indeed, a bound complex with the excess electron occupying the $\nu = +0$ LL in the c_2 of the K valley is such a configuration (see inset Fig. 5d). This is also consistent with the very strong valley polarization η_v of this feature (see Fig. 5f). For densities $n_2 < n < n_3$, the global spin polarization is initially constant and quickly diminishes at n_3 . This behavior is mirrored by the g -factor of X'^- . Increasing the carrier concentration in this regime reduces the g -factor to a minimum value of ~ -5 at n_3 . Strikingly, at exactly this concentration, a change in the scaling of the X'^- binding energy $E_B = E(X^-) - E(X'^-)$ occurs, changing from a linear to a sub-linear dependence with E_F (see Fig. 5d). Moreover, at the same density η_v starts decreasing. For densities $n > n_3$, all valleys and electron spin species are available (see Fig. 5e) since E_F is situated well within c_2 , consistent with a decrease in η_v . The electron concentration approaches the Mott density³⁴ where strong many-body effects start to dominate the interaction of X'^- and electrons of all spins forming a strongly dressed many-body state (see inset Fig. 5d). At such densities, all spin species are available, rendering spin scattering possible since spins of either orientation from all bands can be exchanged with little or no energetic cost. In such a high density regime, the precise local spin structure becomes less relevant, and mean field-"like" theories become applicable. A detailed description of this state calls for dedicated many-body calculations of the spin susceptibility, moving beyond the scope of the present manuscript.

VII. CONCLUSION

Our results show that the spin structure of all excitons in 2D materials are many-body correlated states that have a magneto-optical response that is sensitive to the local carrier density and related spin and valley textures. Moreover, our results strongly suggest that the variation of exciton g -factors in the literature is due to the sensitivity towards excess carrier concentration and interactions of the excitons with the spin and valley texture of local charge. The findings of our study represent an important step towards studying and engineering exciting many-body related phases and novel interaction phenomena in atomically thin materials.

VIII. ACKNOWLEDGEMENTS

Supported by Deutsche Forschungsgemeinschaft (DFG) through the TUM International Graduate School of Science and Engineering (IGSSE) and the German Excellence Cluster-MCQST and e-conversion. We gratefully acknowledge financial support by the PhD program ExQM of the Elite Network of Bavaria. We also gratefully acknowledge financial support from the European Union's Horizon 2020 research and innovation programme under grant agreement No. 820423 (S2QUIP) the German Federal Ministry of Education and Research via the funding program Photonics Research Germany (contracts number 13N14846) and the Bavarian Academy of Sciences and Humanities. M.F., A.S. and F.J. were supported by the Deutsche Forschungsgemeinschaft (DFG) within RTG 2247 and through a grant for CPU time at the HLRN (Berlin/Göttingen). J.K. acknowledges support by the Alexander von Humboldt foundation. J.J.F and A.H. acknowledge support from the Technical University of Munich - Institute for Advanced Study, funded by the German Excellence Initiative and the European Union FP7 under grant agreement 291763 and the German Excellence Strategy Munich Center for Quantum Science and Technology (MCQST). K.W. and T.T. acknowledge support from the Elemental Strategy Initiative conducted by the MEXT, Japan, Grant Number JPMXP0112101001, JSPS KAKENHI Grant Number JP20H00354 and the CREST(JPMJCR15F3), JST. The work has been partially supported by the EC Graphene Flagship project (no. 604391), by the ANR projects ANR-17-CE24-0030 and ANR-19-CE09-0026. M.F., A.S. and F.J. thank Gunnar Schönhoff, Malte Rösner and Tim Wehling for providing material-realistic band structures and bare as well as screened Coulomb matrix elements. We further thank Scott Crooker and Mark Goerbig for insightful and stimulating discussions.

IX. AUTHOR CONTRIBUTIONS

J.K., A.Hö., A.H., M.P., C.F., J.J.F. and A.V.S. conceived and designed the experiments, A.Hö. and J.K. prepared the samples, K.W. and T.T. provided high-quality hBN bulk crystals, J.K., A.Hö., A.D., C.F.

and A.V.S. performed the optical measurements, J.K. and A.V.S. analyzed the data, M.F., A.S. and F.J. computed trion fine-structure, J.K., A.V.S and J.J.F. wrote the manuscript with input from all co-authors.

-
- * jpklein@mit.edu
 † finley@wsi.tum.de
 ‡ andreas.stier@wsi.tum.de
- ¹ Massignan, P., Zaccanti, M. & Bruun, G. M. Polarons, dressed molecules and itinerant ferromagnetism in ultracold fermi gases. *Reports on Progress in Physics* **77**, 034401 (2014). URL <https://doi.org/10.1088/0034-4885/77/3/034401>.
 - ² Bloch, I., Dalibard, J. & Zwerger, W. Many-body physics with ultracold gases. *Reviews of Modern Physics* **80**, 885–964 (2008). URL <https://doi.org/10.1103/revmodphys.80.885>.
 - ³ Boll, M. *et al.* Spin- and density-resolved microscopy of antiferromagnetic correlations in fermi-hubbard chains. *Science* **353**, 1257–1260 (2016). URL <https://doi.org/10.1126/science.aag1635>.
 - ⁴ Mazurenko, A. *et al.* A cold-atom fermi-hubbard antiferromagnet. *Nature* **545**, 462–466 (2017). URL <https://doi.org/10.1038/nature22362>.
 - ⁵ Koepsell, J. *et al.* Imaging magnetic polarons in the doped fermi-hubbard model. *Nature* **572**, 358–362 (2019). URL <https://doi.org/10.1038/s41586-019-1463-1>.
 - ⁶ Fey, C., Schmelcher, P., Imamoglu, A. & Schmidt, R. Theory of exciton-electron scattering in atomically thin semiconductors. *Physical Review B* **101** (2020). URL <https://doi.org/10.1103/physrevb.101.195417>.
 - ⁷ Glazov, M. M. Optical properties of charged excitons in two-dimensional semiconductors (2020). 2004.13484.
 - ⁸ Chen, W. *et al.* Interaction of magnetoexcitons and two-dimensional electron gas in the quantum hall regime. *Physical Review Letters* **64**, 2434–2437 (1990). URL <https://doi.org/10.1103/physrevlett.64.2434>.
 - ⁹ Goldberg, B. B., Heiman, D., Pinczuk, A., Pfeiffer, L. & West, K. Optical investigations of the integer and fractional quantum hall effects: Energy plateaus, intensity minima, and line splitting in band-gap emission. *Physical Review Letters* **65**, 641–644 (1990). URL <https://doi.org/10.1103/physrevlett.65.641>.
 - ¹⁰ Zhu, J., Stormer, H. L., Pfeiffer, L. N., Baldwin, K. W. & West, K. W. Spin susceptibility of an ultra-low-density two-dimensional electron system. *Physical Review Letters* **90** (2003). URL <https://doi.org/10.1103/physrevlett.90.056805>.
 - ¹¹ Gunawan, O. *et al.* Valley susceptibility of an interacting two-dimensional electron system. *Physical Review Letters* **97** (2006). URL <https://doi.org/10.1103/physrevlett.97.186404>.
 - ¹² Sarma, S. D., Hwang, E. H. & Li, Q. Valley-dependent many-body effects in two-dimensional semiconductors. *Physical Review B* **80** (2009). URL <https://doi.org/10.1103/physrevb.80.121303>.
 - ¹³ Nomura, K. & MacDonald, A. H. Quantum hall ferromagnetism in graphene. *Physical Review Letters* **96** (2006). URL <https://doi.org/10.1103/physrevlett.96.256602>.
 - ¹⁴ Young, A. F. *et al.* Spin and valley quantum hall ferromagnetism in graphene. *Nature Physics* **8**, 550–556 (2012). URL <https://doi.org/10.1038/nphys2307>.
 - ¹⁵ Chernikov, A. *et al.* Exciton binding energy and nonhydrogenic rydberg series in monolayer WS₂. *Physical Review Letters* **113** (2014). URL <https://doi.org/10.1103/physrevlett.113.076802>.
 - ¹⁶ Stier, A. *et al.* Magneto-optics of exciton rydberg states in a monolayer semiconductor. *Physical Review Letters* **120** (2018). URL <https://doi.org/10.1103/physrevlett.120.057405>.
 - ¹⁷ Mak, K. F. *et al.* Tightly bound trions in monolayer mos₂. *Nature Materials* **12**, 207–211 (2013). URL <https://doi.org/10.1038/nmat3505>.
 - ¹⁸ Chernikov, A. *et al.* Electrical tuning of exciton binding energies in MonolayerWS₂. *Physical Review Letters* **115** (2015). URL <https://doi.org/10.1103/physrevlett.115.126802>.
 - ¹⁹ Gustafsson, M. V. *et al.* Ambipolar landau levels and strong band-selective carrier interactions in monolayer WSe₂. *Nature Materials* **17**, 411–415 (2018). URL <https://doi.org/10.1038/s41563-018-0036-2>.
 - ²⁰ Huang, B. *et al.* Layer-dependent ferromagnetism in a van der waals crystal down to the monolayer limit. *Nature* **546**, 270–273 (2017). URL <https://doi.org/10.1038/nature22391>.
 - ²¹ Tang, Y. *et al.* Simulation of hubbard model physics in WSe₂/WS₂ moiré superlattices. *Nature* **579**, 353–358 (2020). URL <https://doi.org/10.1038/s41586-020-2085-3>.
 - ²² Shimazaki, Y. *et al.* Strongly correlated electrons and hybrid excitons in a moiré heterostructure. *Nature* **580**, 472–477 (2020). URL <https://doi.org/10.1038/s41586-020-2191-2>.
 - ²³ Regan, E. C. *et al.* Mott and generalized wigner crystal states in WSe₂/WS₂ moiré superlattices. *Nature* **579**, 359–363 (2020). URL <https://doi.org/10.1038/s41586-020-2092-4>.
 - ²⁴ Xiao, D., Liu, G.-B., Feng, W., Xu, X. & Yao, W. Coupled spin and valley physics in monolayers of MoS₂ and other group-VI dichalcogenides. *Physical Review Letters* **108** (2012). URL <https://doi.org/10.1103/physrevlett.108.196802>.
 - ²⁵ Xu, X., Yao, W., Xiao, D. & Heinz, T. F. Spin and pseudospins in layered transition metal dichalcogenides. *Nature Physics* **10** (2014). URL <https://doi.org/10.1038/nphys2942>.
 - ²⁶ Aivazian, G. *et al.* Magnetic control of valley pseudospin in monolayer WSe₂. *Nature Physics* **11**, 148–152 (2015). URL <https://doi.org/10.1038/nphys3201>.

- ²⁷ Srivastava, A. *et al.* Valley zeeman effect in elementary optical excitations of monolayer WSe₂. *Nature Physics* **11**, 141–147 (2015). URL <https://doi.org/10.1038/nphys3203>.
- ²⁸ MacNeill, D. *et al.* Breaking of valley degeneracy by magnetic field in monolayer MoSe₂. *Physical Review Letters* **114** (2015). URL <https://doi.org/10.1103/physrevlett.114.037401>.
- ²⁹ Li, Y. *et al.* Valley splitting and polarization by the zeeman effect in monolayer MoSe₂. *Physical Review Letters* **113** (2014). URL <https://doi.org/10.1103/physrevlett.113.266804>.
- ³⁰ Wang, Z., Shan, J. & Mak, K. F. Valley- and spin-polarized landau levels in monolayer WSe₂. *Nature Nanotechnology* **12**, 144–149 (2016). URL <https://doi.org/10.1038/nnano.2016.213>.
- ³¹ Smoleński, T. *et al.* Interaction-induced shubnikov–de haas oscillations in optical conductivity of monolayer MoSe₂. *Physical Review Letters* **123** (2019). URL <https://doi.org/10.1103/physrevlett.123.097403>.
- ³² Liu, E. *et al.* Landau-quantized excitonic absorption and luminescence in a monolayer valley semiconductor. *Physical Review Letters* **124** (2020). URL <https://doi.org/10.1103/physrevlett.124.097401>.
- ³³ Wang, T. *et al.* Observation of quantized exciton energies in monolayer WSe₂ under a strong magnetic field. *Physical Review X* **10** (2020). URL <https://doi.org/10.1103/physrevx.10.021024>.
- ³⁴ Steinhoff, A. *et al.* Exciton fission in monolayer transition metal dichalcogenide semiconductors. *Nature Communications* **8** (2017). URL <https://doi.org/10.1038/s41467-017-01298-6>.
- ³⁵ Sidler, M. *et al.* Fermi polaron-polaritons in charge-tunable atomically thin semiconductors. *Nature Physics* **13**, 255–261 (2016). URL <https://doi.org/10.1038/nphys3949>.
- ³⁶ Ravets, S. *et al.* Polaron polaritons in the integer and fractional quantum hall regimes. *Physical Review Letters* **120** (2018). URL <https://doi.org/10.1103/physrevlett.120.057401>.
- ³⁷ Pisoni, R. *et al.* Interactions and magnetotransport through spin-valley coupled landau levels in monolayer MoS₂. *Physical Review Letters* **121** (2018). URL <https://doi.org/10.1103/physrevlett.121.247701>.
- ³⁸ Movva, H. C. *et al.* Density-dependent quantum hall states and zeeman splitting in monolayer and bilayer WSe₂. *Physical Review Letters* **118** (2017). URL <https://doi.org/10.1103/physrevlett.118.247701>.
- ³⁹ Xu, S. *et al.* Odd-integer quantum hall states and giant spin susceptibility in p-type few-layer WSe₂. *Physical Review Letters* **118** (2017). URL <https://doi.org/10.1103/physrevlett.118.067702>.
- ⁴⁰ Larentis, S. *et al.* Large effective mass and interaction-enhanced zeeman splitting of k-valley electrons in MoSe₂. *Physical Review B* **97** (2018). URL <https://doi.org/10.1103/physrevb.97.201407>.
- ⁴¹ Fallahzad, B. *et al.* Shubnikov–de haas oscillations of high-mobility holes in monolayer and bilayer WSe₂: Landau level degeneracy, effective mass, and negative compressibility. *Physical Review Letters* **116** (2016). URL <https://doi.org/10.1103/physrevlett.116.086601>.
- ⁴² Lin, J. *et al.* Determining interaction enhanced valley susceptibility in spin-valley-locked MoS₂. *Nano Letters* **19**, 1736–1742 (2019). URL <https://doi.org/10.1021/acs.nanolett.8b04731>.
- ⁴³ Deilmann, T. & Thygesen, K. S. Dark excitations in monolayer transition metal dichalcogenides. *Physical Review B* **96** (2017). URL <https://doi.org/10.1103/physrevb.96.201113>.
- ⁴⁴ Robert, C. *et al.* Measurement of the spin-forbidden dark excitons in MoS₂ and MoSe₂ monolayers. *arXiv preprint arXiv:2002.03877* (2020).
- ⁴⁵ Volmer, F. *et al.* How the dynamic of photo-induced gate screening complicates the investigation of valley physics in 2d materials. *arXiv preprint arXiv:2006.04775* (2020).
- ⁴⁶ Klein, J. *et al.* Impact of substrate induced band tail states on the electronic and optical properties of MoS₂. *Applied Physics Letters* **115**, 261603 (2019). URL <https://doi.org/10.1063/1.5131270>.
- ⁴⁷ Wierzbowski, J. *et al.* Direct exciton emission from atomically thin transition metal dichalcogenide heterostructures near the lifetime limit. *Scientific Reports* **7** (2017). URL <https://doi.org/10.1038/s41598-017-09739-4>.
- ⁴⁸ Cadiz, F. *et al.* Excitonic linewidth approaching the homogeneous limit in MoS₂-based van der waals heterostructures. *Physical Review X* **7** (2017). URL <https://doi.org/10.1103/physrevx.7.021026>.
- ⁴⁹ Florian, M. *et al.* The dielectric impact of layer distances on exciton and trion binding energies in van der waals heterostructures. *Nano Letters* **18**, 2725–2732 (2018). URL <https://doi.org/10.1021/acs.nanolett.8b00840>.
- ⁵⁰ Wang, G. *et al.* Magneto-optics in transition metal diselenide monolayers. *2D Materials* **2**, 034002 (2015). URL <https://doi.org/10.1088/2053-1583/2/3/034002>.
- ⁵¹ Stier, A. V., McCreary, K. M., Jonker, B. T., Kono, J. & Crooker, S. A. Exciton diamagnetic shifts and valley zeeman effects in monolayer WS₂ and MoS₂ to 65 tesla. *Nature Communications* **7** (2016). URL <https://doi.org/10.1038/ncomms10643>.
- ⁵² Goryca, M. *et al.* Revealing exciton masses and dielectric properties of monolayer semiconductors with high magnetic fields. *Nature Communications* **10** (2019). URL <https://doi.org/10.1038/s41467-019-12180-y>.
- ⁵³ Deilmann, T., Krüger, P. & Rohlfing, M. Ab initio studies of exciton g factors: Monolayer transition metal dichalcogenides in magnetic fields. *Physical Review Letters* **124** (2020). URL <https://doi.org/10.1103/physrevlett.124.226402>.
- ⁵⁴ Jadcak, J. *et al.* Fine structure of negatively charged and neutral excitons in monolayer MoS₂. *arXiv preprint arXiv:2001.07929* (2020).
- ⁵⁵ Mitioglu, A. A. *et al.* Magnetoexcitons in large area CVD-grown monolayer MoS₂ and MoSe₂ on sapphire. *Physical Review B* **93** (2016). URL <https://doi.org/10.1103/physrevb.93.165412>.
- ⁵⁶ Wang, Z., Mak, K. F. & Shan, J. Strongly interaction-enhanced valley magnetic response in monolayer WSe₂. *Physical Review Letters* **120** (2018). URL <https://doi.org/10.1103/physrevlett.120.066402>.
- ⁵⁷ Jovanov, V. *et al.* Observation and explanation of strong electrically tunable exciton factors in composition engineered In(Ga)As quantum dots. *Physical Review B* **83** (2011). URL <https://doi.org/10.1103/physrevb.83.161303>.
- ⁵⁸ Furdyna, J. K. Diluted magnetic semiconductors. *Journal of Applied Physics* **64**, R29–R64 (1988). URL <https://doi.org/10.1063/1.341700>.
- ⁵⁹ Seyler, K. L. *et al.* Valley manipulation by optically tuning the magnetic proximity effect in WSe₂/CrI₃ het-

- erostructures. *Nano Letters* **18** (2018). URL <https://doi.org/10.1021/acs.nanolett.8b01105>.
- ⁶⁰ Norden, T. *et al.* Giant valley splitting in monolayer WS₂ by magnetic proximity effect. *Nature Communications* **10** (2019). URL <https://doi.org/10.1038/s41467-019-11966-4>.
- ⁶¹ Yu, H., Liu, G.-B., Gong, P., Xu, X. & Yao, W. Dirac cones and dirac saddle points of bright excitons in monolayer transition metal dichalcogenides. *Nature Communications* **5** (2014). URL <https://doi.org/10.1038/ncomms4876>.
- ⁶² Jones, A. M. *et al.* Excitonic luminescence upconversion in a two-dimensional semiconductor. *Nature Physics* **12**, 323–327 (2015). URL <https://doi.org/10.1038/nphys3604>.
- ⁶³ Plechinger, G. *et al.* Trion fine structure and coupled spin–valley dynamics in monolayer tungsten disulfide. *Nature Communications* **7** (2016). URL <https://doi.org/10.1038/ncomms12715>.
- ⁶⁴ Courtade, E. *et al.* Charged excitons in monolayer WSe₂: Experiment and theory. *Physical Review B* **96** (2017). URL <https://doi.org/10.1103/physrevb.96.085302>.
- ⁶⁵ Drüppel, M., Deilmann, T., Krüger, P. & Rohlfing, M. Diversity of trion states and substrate effects in the optical properties of an MoS₂ monolayer. *Nature Communications* **8** (2017). URL <https://doi.org/10.1038/s41467-017-02286-6>.
- ⁶⁶ Attaccalite, C., Moroni, S., Gori-Giorgi, P. & Bachelet, G. B. Correlation energy and spin polarization in the 2d electron gas. *Physical Review Letters* **88** (2002). URL <https://doi.org/10.1103/physrevlett.88.256601>.
- ⁶⁷ Rose, F., Goerbig, M. O. & Piéchon, F. Spin- and valley-dependent magneto-optical properties of MoS₂. *Physical Review B* **88** (2013). URL <https://doi.org/10.1103/physrevb.88.125438>.
- ⁶⁸ Kormányos, A. *et al.* $k \cdot p$ theory for two-dimensional transition metal dichalcogenide semiconductors. *2D Materials* **2**, 022001 (2015). URL <https://doi.org/10.1088/2053-1583/2/2/022001>.
- ⁶⁹ Bertoni, R. *et al.* Generation and evolution of spin-, valley-, and layer-polarized excited carriers in inversion-symmetric WSe₂. *Physical Review Letters* **117** (2016). URL <https://doi.org/10.1103/physrevlett.117.277201>.
- ⁷⁰ Lyons, T. P. *et al.* The valley zeeman effect in inter- and intra-valley trions in monolayer WSe₂. *Nature Communications* **10** (2019). URL <https://doi.org/10.1038/s41467-019-10228-7>.
- ⁷¹ Latta, C. *et al.* Quantum quench of kondo correlations in optical absorption. *Nature* **474**, 627–630 (2011). URL <https://doi.org/10.1038/nature10204>.
- ⁷² Roch, J. G. *et al.* Spin-polarized electrons in monolayer MoS₂. *Nature Nanotechnology* **14**, 432–436 (2019). URL <https://doi.org/10.1038/s41565-019-0397-y>.
- ⁷³ Palmieri, T. *et al.* Mahan excitons in room-temperature methylammonium lead bromide perovskites. *Nature Communications* **11** (2020). URL <https://doi.org/10.1038/s41467-020-14683-5>.
- ⁷⁴ Tuan, D. V., Scharf, B., Žutić, I. & Dery, H. Marrying excitons and plasmons in monolayer transition-metal dichalcogenides. *Physical Review X* **7** (2017). URL <https://doi.org/10.1103/physrevx.7.041040>.

Supplemental Material - Quantized many-body spin-valley textures in charge tunable monolayer MoS₂

J. Klein*

*Walter Schottky Institut and Physik Department, Technische Universität München,
Am Coulombwall 4, 85748 Garching, Germany and
Department of Materials Science and Engineering,
Massachusetts Institute of Technology,
Cambridge, Massachusetts 02139, USA*

A. Hötger, A. W. Holleitner, J. J. Finley,[†] and A. V. Stier[‡]

*Walter Schottky Institut and Physik Department,
Technische Universität München, Am Coulombwall 4, 85748 Garching, Germany*

M. Florian, A. Steinhoff, and F. Jahnke

*Institut für Theoretische Physik, Universität Bremen,
P.O. Box 330 440, 28334 Bremen, Germany*

A. Delhomme, M. Potemski, and C. Faugeras

*Université Grenoble Alpes, INSA Toulouse,
Univ. Toulouse Paul Sabatier, EMFL,
CNRS, LNCMI, 38000 Grenoble, France.*

T. Taniguchi and K. Watanabe

*Research Center for Functional Materials,
National Institute for Materials Science,
1-1 Namiki, Tsukuba 305-0044, Japan*

(Dated: 2020-07-31)

* jpklein@mit.edu

† finley@wsi.tum.de

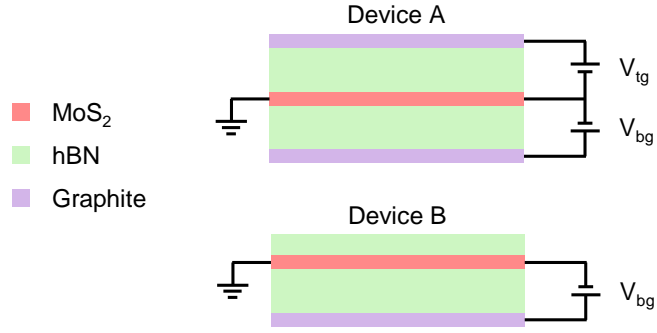
‡ andreas.stier@wsi.tum.de

CONTENTS

I. Field-effect device for carrier density control in monolayer MoS ₂	4
II. Transfer characteristics in high magnetic fields	6
III. Trion fine structure in monolayer MoS ₂ from theory	7
IV. Carrier density dependent magneto-photoluminescence of monolayer MoS ₂	11
V. Landau levels in the negatively charged <i>intravalley</i> trion	12
VI. Extracting the electron mass from Landau levels observed in the trion PL	14
VII. Calculating the density dependent hole mass	16
VIII. Quantized spin-valley texture	18
IX. Valley Zeeman shift of X^- , X^+ and X'^-	20
X. Magnetic field and density dependent valley dichroism	21
XI. Magnetic moment of Bloch electrons: lattice Hamiltonian vs. atomic contributions	23
References	28

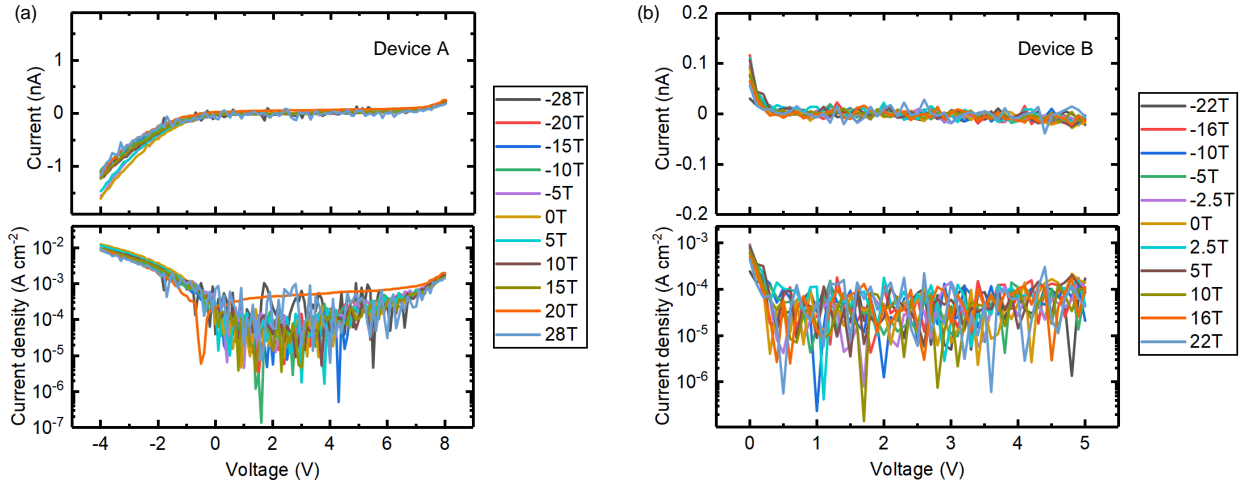
I. FIELD-EFFECT DEVICE FOR CARRIER DENSITY CONTROL IN MONOLAYER MoS_2

We make use of field-effect devices to control the carrier density in monolayer MoS_2 . [1] SI Figure 1 shows the two device geometries used in this manuscript. In both devices, monolayer MoS_2 is encapsulated in hBN. We use the hBN for two main reasons: (i) Encapsulation reduces inhomogeneous linewidth broadening of excitons [2] and (ii) as gate dielectric that withstands high breakdown fields, [3] thus preventing leakage currents. We use few-layer graphite as the gate-electrode and to directly contact the MoS_2 . Sample A is a dual-gate device with top and bottom gates as shown in SI Fig. 1(a) while device B is a single-gated. In device A, equal gate voltages with the same polarity are applied to the gates $V_{bg} = V_{tg}$ with respect to the monolayer MoS_2 , thus controlling the carrier density. In the dual-gated device A, we are also able to tune from the n- into the p-doped regime, while in device B, we can tune from the intrinsic regime to the n-doped regime only. The observation that only the n-doped regime is accessible with a single-gate is common in the literature for monolayer MoS_2 . [4, 5] It is likely that the dual-gate device allows to access the p-doped regime since it overcomes Fermi-level pinning effects by the symmetric device geometry. Furthermore, dual gates allow larger applied effective fields for tuning the carrier density. We determine the carrier density by using a simple plate capacitor model where the device capacitance is $C = \epsilon_0 \epsilon_{hBN} / d$ with the dielectric constant of multilayer hBN $\epsilon_{hBN} = 2.5$ [3, 6–8] and the hBN layer thickness d which is determined by atomic force microscopy. The carrier density is given by $n = CV_{bg}/e$ for the single-gate device. Since top and bottom hBN thickness are very similar for the dual-gate device we relate the carrier density with the gate voltage through $n = C(V_{tg} + V_{bg})/e = 2CV/e$.



SI Figure 1. Schematic of the field-effect van der Waals devices used throughout this manuscript. For both devices, monolayer MoS₂ is encapsulated between hBN. Device *A* is a single-gate device where a graphene bottom gate is used for applying a bias voltage V_{bg} . Device *B* is a dual-gate device where the carrier density is controlled with a top- and bottom-gate V_{tg} and V_{bg} . The same voltage with same polarity is applied to both gates for enhancing the gating effect.

II. TRANSFER CHARACTERISTICS IN HIGH MAGNETIC FIELDS



SI Figure 2. Transfer characteristics of (a) dual-gate device *A* and (b) single-gate device *B*. Top panels: I-V curves for all magnetic fields applied. Bottom panels: Current density as a function of applied bias voltage ($V = V_{bg} = V_{tg}$). The monolayer MoS₂ is excited with 30 μ W at 514 nm with a laser spot diameter at the sample of $\sim 4 \mu$ m.

For the gate-dependent magneto-photoluminescence measurements on device *A* and *B*, we apply a magnetic field and vary the gate voltage in steps of 100 mV while collecting PL spectra for every gate voltage step. We perform the same gate biasing sequence for every magnetic field, thus ensuring that the voltage sweeps at different magnetic fields are directly comparable. We first apply a static magnetic field and then we tune the bias voltage from max. V_+ to max. V_- . Typical current voltage characteristics of device *A* and *B* are presented in SI Fig. 2(a) and (b). For device *A*, we apply equal voltage to top- and bottom-gate ($V = V_{bg} = V_{tg}$). From the transfer characteristics of both devices, we find that our biasing scheme is highly reproducible for all magnetic fields applied in the experiment. The reproducibility is due to the graphite contacts to the MoS₂ which is known for low contact resistance and small Schottky barrier heights. [9, 10] The leakage currents are in the noise floor for most of the range and negligible leakage currents of < 1.5 nA, that correspond to current densities of $< 10^{-2}$ A cm⁻², at the highest bias voltages. The data are collected for a laser excitation power of 30 μ W with a laser excitation energy of 2.41 eV.

III. TRION FINE STRUCTURE IN MONOLAYER MoS_2 FROM THEORY

The linear absorption spectrum of MoS_2 is calculated by solving the semiconductor Bloch equations (SBE) for the microscopic interband polarizations $\psi_{\mathbf{k}}^{he} = \langle a_{\mathbf{k}}^h a_{\mathbf{k}}^e \rangle$, where the operators $a_{\mathbf{k}}^\lambda$ annihilate a carrier in band λ with momentum \mathbf{k} . In the limit of vanishing excitation/doping density, the SBE become formally equivalent to the Bethe-Salpeter equation [11] and read in Fourier space

$$(\varepsilon_{\mathbf{k}}^e + \varepsilon_{\mathbf{k}}^h - \hbar\omega)\psi_{\mathbf{k}}^{he}(\omega) - \frac{1}{A} \sum_{\mathbf{k}'} \sum_{h'e'} \left(V_{\mathbf{k},\mathbf{k}',\mathbf{k},\mathbf{k}'}^{eh'h'e'} - U_{\mathbf{k},\mathbf{k}',\mathbf{k}',\mathbf{k}}^{eh'e'h} \right) \psi_{\mathbf{k}'}^{h'e'}(\omega) = (d_{\mathbf{k}}^{he})^* E(\omega), \quad (1)$$

with bandstructures $\varepsilon_{\mathbf{k}}^{e/h}$, Coulomb matrix elements $V_{\mathbf{k}+\mathbf{q},\mathbf{k}'-\mathbf{q},\mathbf{k},\mathbf{k}}$ and dipole matrix elements $d_{\mathbf{k}}^{he}$ that are projected in the polarization direction of the electric field $E(t)$, which is assumed to propagate vertical to the single-layer plane. A denotes the crystal area. Note that the electron-hole exchange interaction in Eq. (1) is described by unscreened Coulomb matrix elements U [12–14], while V denotes Coulomb matrix elements that are screened by carriers in occupied bands and the dielectric environment of the TMDC layer. The linear response of the material is given by the macroscopic susceptibility $\chi(\omega) = \frac{1}{A} \sum_{\mathbf{k}} \sum_{he} (d_{\mathbf{k}}^{he} \psi_{\mathbf{k}}^{he} + c.c.) / E(\omega)$, which contains excitons as discrete resonances below a continuum of optical interband transitions.

At moderate charge carrier densities, signatures of tightly bound trions additionally appear in experimental spectra. To capture this effect, we extend the semiconductor Bloch equations presented in Eq. (1) and explicitly include correlation functions that describe three-particle states. For this purpose, we examine the equation of motion for the microscopic polarization for finite electron density, which reads

$$\begin{aligned} & (\varepsilon_{\mathbf{k}}^e + \varepsilon_{\mathbf{k}}^h - \hbar\omega)\Psi_{\mathbf{k}}^{he}(\omega) - \frac{1}{A} \sum_{\mathbf{k}'} \sum_{h'e'} \left(V_{\mathbf{k},\mathbf{k}',\mathbf{k},\mathbf{k}'}^{eh'h'e'} - U_{\mathbf{k},\mathbf{k}',\mathbf{k}',\mathbf{k}}^{eh'e'h} \right) \Psi_{\mathbf{k}'}^{h'e'}(\omega) \\ & + \frac{1}{A^2} \sum_{\mathbf{Q}\mathbf{q}} \sum_{e_2 h_3 e_4} \left(V_{\mathbf{Q},\mathbf{k}-\mathbf{q},\mathbf{k},\mathbf{Q}-\mathbf{q}}^{e_2 h_3 h e_4} - U_{\mathbf{Q},\mathbf{k}-\mathbf{q},\mathbf{Q}-\mathbf{q},\mathbf{k}}^{e_2 h_3 e_4 h} \right) T_{e_4 h_3 e_2}(\mathbf{k}, \mathbf{Q} - \mathbf{q}, \mathbf{Q}) \\ & - \frac{1}{A^2} \sum_{\mathbf{Q}\mathbf{q}} \sum_{e_2 e_3 e_4} \left(V_{\mathbf{Q},\mathbf{k},\mathbf{k}+\mathbf{q},\mathbf{Q}-\mathbf{q}}^{e_2 e_4 e_3} - V_{\mathbf{Q},\mathbf{k},\mathbf{Q}-\mathbf{q},\mathbf{k}+\mathbf{q}}^{e_2 e_3 e_4} \right) T_{e_4 e_3 h e_2}(\mathbf{k} + \mathbf{q}, \mathbf{Q} - \mathbf{q}, \mathbf{Q}) \\ & = (1 - f_{\mathbf{k}}^e)(d_{\mathbf{k}}^{he})^* E(\omega). \end{aligned} \quad (2)$$

Here, $f_{\mathbf{k}}^\lambda$ denotes the carrier population in the band λ . We assume the system to be in thermal quasi-equilibrium described by Fermi functions with given temperature and carrier

density. The Coulomb interaction couples the polarization Ψ^{he} to the trion amplitude

$$T_{e_1 e_2 h_3 e_4}(\mathbf{k}_1, \mathbf{k}_2, \mathbf{Q}) = \langle a_{\mathbf{Q}}^{e_4 \dagger} a_{-(\mathbf{k}_1 + \mathbf{k}_2 - \mathbf{Q})}^{h_3} a_{\mathbf{k}_2}^{e_2} a_{\mathbf{k}_1}^{e_1} \rangle, \quad (3)$$

which is a four-operator expectation value and describes the correlated process of annihilating two electrons and one hole, leaving behind an electron with momentum \mathbf{Q} in the conduction band and is linked to the optical response of an electron trion X^- . For moderate carrier density and linear optics a closed expression for the trion amplitudes can be obtain [15, 16]

$$\begin{aligned} & (\varepsilon_{\mathbf{k}_1}^{e_1} + \varepsilon_{\mathbf{k}_2}^{e_2} + \varepsilon_{\mathbf{k}_3}^{h_3} - \varepsilon_{\mathbf{Q}}^{e_4} - \hbar\omega) T_{e_1 e_2 h_3 e_4}(\mathbf{k}_1, \mathbf{k}_2, \mathbf{Q}) \\ & - \frac{1}{A} \sum_{\mathbf{q}} \sum_{h_5, e_6} (V_{\mathbf{k}_2, \mathbf{k}_3 - \mathbf{q}, \mathbf{k}_3, \mathbf{k}_2 - \mathbf{q}}^{e_2 h_5 h_3 e_6} - U_{\mathbf{k}_2, \mathbf{k}_3 - \mathbf{q}, \mathbf{k}_2 - \mathbf{q}, \mathbf{k}_3}^{e_2 h_5 e_6 h_3}) T_{e_1 e_6 h_5 e_4}(\mathbf{k}_1, \mathbf{k}_2 - \mathbf{q}, \mathbf{Q}) \\ & - \frac{1}{A} \sum_{\mathbf{q}} \sum_{h_5, e_6} (V_{\mathbf{k}_1, \mathbf{k}_3 - \mathbf{q}, \mathbf{k}_3, \mathbf{k}_1 - \mathbf{q}}^{e_1 h_5 h_3 e_6} - U_{\mathbf{k}_1, \mathbf{k}_3 - \mathbf{q}, \mathbf{k}_1 - \mathbf{q}, \mathbf{k}_3}^{e_1 h_5 e_6 h_3}) T_{e_6 e_2 h_5 e_4}(\mathbf{k}_1 - \mathbf{q}, \mathbf{k}_2, \mathbf{Q}) \\ & + \frac{1}{A} \sum_{\mathbf{q}} \sum_{e_5, e_6} (V_{\mathbf{k}_1, \mathbf{k}_2, \mathbf{k}_2 + \mathbf{q}, \mathbf{k}_1 - \mathbf{q}}^{e_1 e_2 e_5 e_6} - V_{\mathbf{k}_1, \mathbf{k}_2, \mathbf{k}_1 - \mathbf{q}, \mathbf{k}_2 + \mathbf{q}}^{e_1 e_2 e_6 e_5}) T_{e_6 e_5 h_3 e_4}(\mathbf{k}_1 - \mathbf{q}, \mathbf{k}_2 + \mathbf{q}, \mathbf{Q}) \\ & = f_{\mathbf{Q}}^{e_1} (d_{\mathbf{k}_2}^{he} \delta_{\mathbf{k}_1, \mathbf{Q}} \delta_{e, e_1} - d_{\mathbf{k}_1}^{he} \delta_{\mathbf{k}_2, \mathbf{Q}}) E(\omega), \end{aligned} \quad (4)$$

where the homogeneous part of these equations represents a generalized three-particle Schrödinger equation in reciprocal space. The oscillator strength of a transition between a trion state with total momentum \mathbf{Q} and an electron state are directly proportional to the carrier population $f_{\mathbf{Q}}^\lambda$, which is apparent from the inhomogeneous part of Eq. (4). Thus, trions visible in optical spectra are hosted in the K and K' valleys of the two lowest conduction (highest valence) bands to which we limit our single-particle basis.

We combine the above many-body theory of trions with ab-initio methods providing material-realistic band structures and bare as well as screened Coulomb matrix elements on a G_0W_0 level as input for the equations of motion (Eq. (2) and (4)). More details on the G_0W_0 calculations are given in Ref. [17]. First- and second-order Rashba spin-orbit coupling are added subsequently to account for the spin-orbit splitting in the conduction- and the valence-band K valleys, see Ref. [17, 18]. Direct dipole transition matrix elements are calculated using a Peierls approximation [17]. Coulomb matrix elements for hBN encapsulated MoS_2 are obtained in two steps: Bare Coulomb matrix elements for a freestanding monolayer and the RPA dielectric function are calculated in a localized Wannier basis $|\alpha\rangle$ with dominant W-orbital character. Substrate effects are then included using the *Wannier function continuum*

electrostatics (WFCE) approach as described in Refs. [16, 19]. The approach combines a continuum electrostatic model for the screening by the dielectric environment with a localized description of the Coulomb interaction. The actual parametrization is provided in Ref. [16] and has been shown to provide reasonable agreement with experiments. Subsequently, the Coulomb matrix elements are transformed in Bloch-state representation

$$U_{\mathbf{k}+\mathbf{q},\mathbf{k}'-\mathbf{q},\mathbf{k},\mathbf{k}'}^{\lambda_1\lambda_2\lambda_3\lambda_4} = \sum_{\alpha\beta\gamma\delta} [c_{\alpha}^{\lambda_1}(\mathbf{k}+\mathbf{q})]^* [c_{\beta}^{\lambda_2}(\mathbf{k}'-\mathbf{q})]^* c_{\gamma}^{\lambda_3}(\mathbf{k}') c_{\delta}^{\lambda_4}(\mathbf{k}) U_{\mathbf{q}}^{\alpha\beta\gamma\delta}. \quad (5)$$

where the coefficients $c_{\alpha}^{\lambda}(\mathbf{k})$ connect the localized and the Bloch basis, see Eq. (39). As the Coulomb interaction is spin-diagonal, only the electron-hole exchange terms couple trions with different spin combinations and are known to give rise to a fine structure splitting of the trion resonances [20]. A proper description of electron-hole exchange requires matrix elements with density-density-like $U_{\mathbf{q}}^{\alpha\beta\beta\alpha}$ and exchange-like contributions $U^{\alpha\beta\alpha\beta}$ in the local representation [14, 21]. While the density-density-like matrix elements are momentum-dependent and thus nonlocal in real space, the exchange-like matrix elements are practically momentum-independent and correspond to local interaction processes between carriers within the same unit cell. For monolayer MoS₂ we find that the dominant exchange-like matrix elements amount to 0.378 eV (0.20 eV) per unit-cell area for interaction between $d_{m=0}$ and $d_{m=\pm 2}$ (among $d_{m=\pm 2}$) orbitals.

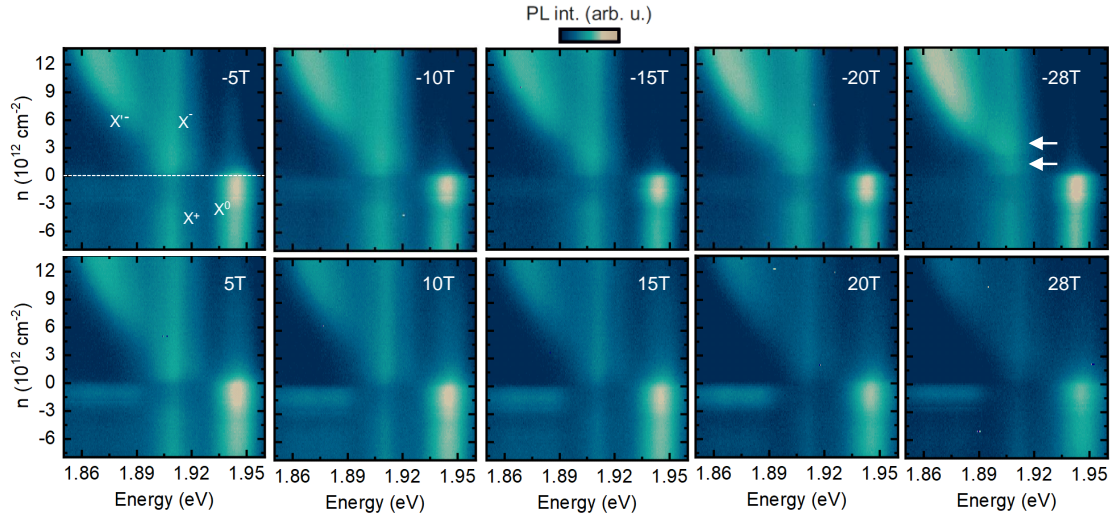
To compute optical absorption spectra numerically, the coupled equations of motion (Eq. (2) and (4)) are solved in frequency space. Due to translational symmetry of the crystal, trions with different total momentum \mathbf{Q} do not couple to each other, thus, we restrict the calculation to the main contribution at the K/K' point. Note that contributions from finite center-of-mass momentum give rise to an asymmetric line shape caused by electron recoil [15]. The first Brillouin zone is sampled by a 84×84 Monkhorst-Pack mesh and a region around the K/K' point defined by a radius of 3.5 nm^{-1} . Due to the numerical discretization of momentum space, there is an uncertainty of binding energies of $\pm 0.5 \text{ meV}$. For the matrix inversion problem we utilize an iterative Krylov-space method as contained in the PETSc toolkit [22].

A qualitative understanding of the trion fine structure can be obtained from a configuration model. The homogenous part of Eq. (4) constitutes a three-particle Hamiltonian whose eigenstates describe trions with total momentum \mathbf{Q} . The Hamiltonian can be split into a part H_0 without electron-hole exchange and an exchange part H_U according to the

Coulomb matrix element. Microscopically, trions can be interpreted as a superposition of an exciton and an electron state with different momenta. Configurations are eigenstates of the three-particle Hamiltonian H_0 that contains the kinetic energies of two electrons and a hole as well as the direct Coulomb interaction. There are six optically bright configurations in the subspace of zero-momentum trions with a hole located in the highest valance band [23]. Due to time-reversal symmetry the configurations are pairwise degenerate and are connected by changing K into K' and flipping all spins. In Fig. 3a of the main text the configurations are shown for $\mathbf{Q} = \mathbf{K}$. By adding electron-hole exchange to this picture, interaction between the configurations is introduced and leads to new eigenstates and -energies. It is the new eigenstates including interaction which are observed in experiment instead of the configurations. It turns out that the non-local exchange, which mixes excitons in the K and K' valleys with finite total momentum, leads to a singlet-triplet splitting of two trion configurations and gives rise to the threefold fine structure observed in the experiment.

IV. CARRIER DENSITY DEPENDENT MAGNETO-PHOTOLUMINESCENCE OF MONOLAYER MoS_2

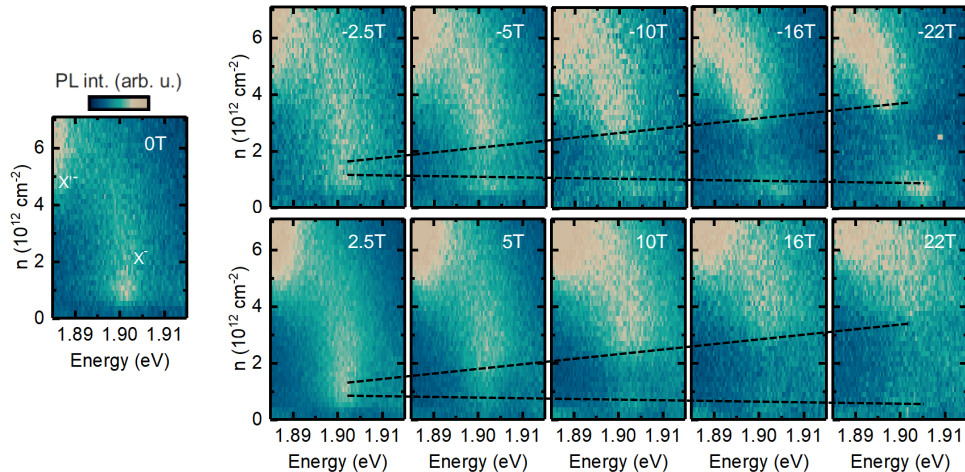
The σ^- circularly polarized, charge carrier density dependent magneto-photoluminescence of device *A* is shown in SI Fig. 3. The above described biasing sequence is used to maintain sample stability throughout the individual voltage sweeps for static magnetic fields ranging from $B = -28 \text{ T}$ to $B = 28 \text{ T}$.



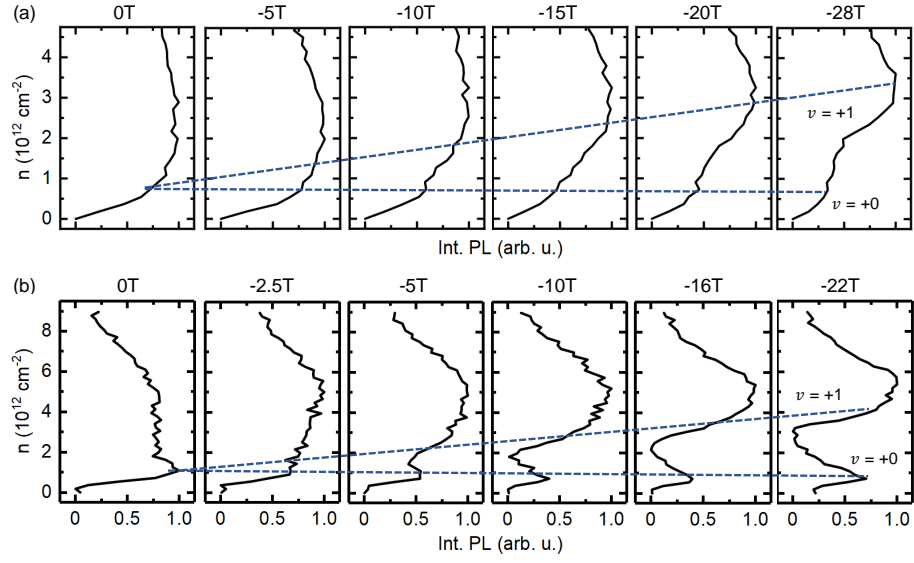
SI Figure 3. Carrier density dependent low-temperature ($T = 5 \text{ K}$) μ -PL for static magnetic fields ranging from -28 T to 28 T . The X^0 , X^- , X^+ and X'^- PL features are marked.

V. LANDAU LEVELS IN THE NEGATIVELY CHARGED *INTRAVALLEY* TRION

SI Figure 4 shows density dependent false color plots of the low-temperature ($T = 5$ K) magneto-PL from device *B*. In particular, the intravalley trion X^- is shown for magnetic fields ranging from -22 T to 22 T. Similar to the *intravalley* trion in device *A*, Landau levels with filling factors $\nu = +0$ and $\nu = +1$ which period increases with the applied magnetic field. The quantum oscillations are analogous to Shubnikov-de-Haas oscillations in transport studies. [24] Here, the position of the LLs is derived from the kinks of the quantum oscillations which are a direct consequence of the Fermi level being tuned in resonance with the individual LL, thus, enhancing trion oscillator strength mediated by carrier scattering. Oppositely, when the Fermi level is situated in between the LLs, no scattering occurs resulting in a reduction of the trion formation rate. This oscillation is clearly visible in the *intravalley* trion X^- in both, device *A* and *B*. SI Figure 5 shows the integrated PL intensity of the X^- as a function of the applied carrier density for static applied magnetic fields. We find the same LL structure in both devices with filling factors of $\nu = +0$ and $\nu = +1$. The LLs vanish in both devices around the same carrier density $n \sim 4 \cdot 10^{12} \text{cm}^{-2}$ which is defined by the situation the Fermi level touches the upper conduction band.



SI Figure 4. Carrier density dependent low-temperature ($T = 5$ K) μ -PL of device *B* for static magnetic fields ranging from 22 T to -22 T of the *intravalley* trion X^- . The dashed lines highlight Landau levels in the X^- with filling factors of $\nu = +0$ and $\nu = +1$. Peaks in the integrated PL correspond to half filling of LLs. [25]



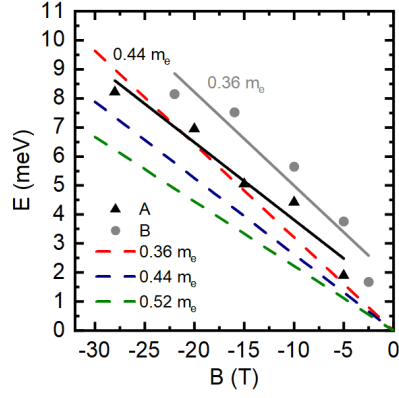
SI Figure 5. (a) Spectrally integrated PL of the intravalley trion X^- as a function of carrier density for device *A* and (b) device *B*. For increasing magnetic fields, LLs emerge with filling factors of $\nu = +0$ and $\nu = +1$ as indicated by the dashed lines.

VI. EXTRACTING THE ELECTRON MASS FROM LANDAU LEVELS OBSERVED IN THE TRION PL

For an electron in a given valley, the energy difference between subsequent LLs in a magnetic field is given by the cyclotron energy

$$E_C = \hbar\omega_C \tag{6}$$

with the cyclotron frequency $\omega_C = eB/m_e$. All contributions from spin and Berry curvature related Zeeman energies cancel out. [26] From our magneto-PL measurements in SI Figure 4, we observe LLs with filling factors $\nu = +0$ and $\nu = +1$. We can calibrate the applied gate voltage into an absolute energy scale by relating the carrier density for which the Fermi level tunes into the upper conduction band c_2 to the dark-bright exciton splitting. In our experiment, the Fermi energy enters c_2 for a density $n = 4 \cdot 10^{12} \text{cm}^{-2}$. At this density, the X'^- PL feature emerges and this emergence has unambiguously been related to E_F in the c_2 band. [24] The dark-bright splitting of the conduction bands has recently been determined to be 14 meV. [24, 27] SI Figure 6 shows the shift of the LL difference as a function of the applied magnetic field for device *A* and *B*. In order to obtain the electron mass, we apply a linear fit to the charge carrier difference between the 0^{th} and 1^{st} LL as a function of magnetic field where we express Δn as an energy by normalizing to the carrier density at which the upper conduction band is reached using the dark-bright splitting $\Delta_{db} = 14 \text{meV}$. Utilizing Eq. 6 yields a value of $m_e = 0.44 \pm 0.15m_0$ ($m_e = 0.36 \pm 0.15m_0$) for device *A* (*B*).



SI Figure 6. Calculated energy shift from the carrier density difference of the LL with filling factor $\nu = +0$ and $\nu = +1$ at negative magnetic field taking into account the spin-orbit splitting of the conduction bands of $\Delta_{db} = 14 \text{ meV}$ [28] and the carrier density at which the Fermi level touches the upper spin-orbit split conduction bands $n_2 = 4 \cdot 10^{12} \text{ cm}^{-2}$.

VII. CALCULATING THE DENSITY DEPENDENT HOLE MASS

We determined the electron mass in device *A* to be $m_e = 0.44 \pm 0.15m_0$. Here, we determine the effective hole mass m_h based on the assumption that the electron mass stays constant up to carrier densities of $5 \cdot 10^{12} \text{cm}^{-2}$. [24] The Zeeman energy of the trion is given by [29]

$$H_Z = \frac{1}{2} \left[\tau_1 g_{ve}^{vb} + s_1 g_s^{vb} + \sum_{i=2}^{N=3} \left(\tau_i g_{ve}^{cb} + s_i g_s^{cb} \right) \right] \mu_B B \quad (7)$$

where the index $i = 1$ is assigned to the bound hole and indices $i = 2, 3$ are assigned to the bound and excess electron of the trion. Here, g_{ve} and g_s are the valley and spin g -factors in the conduction and valence band, respectively. The valley and spin indices are $\tau_i = \pm 1$ ($K = +1$ and $K' = -1$) and $s_i = \pm 1$ ($+1$ spin- \uparrow and -1 spin- \downarrow). The change in the emitted photon energy due to radiative recombination of the negative trion in a magnetic field is [29]

$$\Delta E_{\hbar\omega} = \Delta E_Z - \Delta E_R + \Delta E_D \quad (8)$$

with ΔE_Z the Zeeman shift of the electron-hole pair within the trion, ΔE_R the excess electron recoil shift and ΔE_D the diamagnetic shift. Since in the applied magnetic field range here, the diamagnetic shift is negligible, [26] we omit this term in the following discussions. Unlike neutral exciton recombination, trion recombination cannot be a zero momentum process as the same momentum is imprinted onto the excess electron as recoil, detracting from the absorbed photon energy. The excess electron recoil depends on the temperature and the Fermi energy. The recoil cost is the energy difference in the trion and the free electron in the first LL. The change in energy of the excess electron after trion recombination in a magnetic field is [29]

$$\Delta E_e^\tau = \frac{1}{2} \hbar\omega_c \left(1 - \frac{m_3}{m_T} \right) + \frac{1}{2} \tau_e g_e \mu_B B \quad (9)$$

with the cyclotron energy $\hbar\omega_c = \frac{eB}{m_3}$, the valley index τ_e , the trion effective mass $m_T = \sum_{i=1}^{N=3} m_i$ and the bare electron g -factor g_e . Importantly, this recoil energy cost is equal in both valleys and simplifies to

$$\Delta E_e^\tau = \frac{1}{2} \hbar\omega_c - \frac{1}{2} \hbar\omega_T + \frac{1}{2} \tau_e g_e \mu_B B \quad (10)$$

where the first term describes the final state $|f\rangle$ of the trion, which is an electron in a LL, and the second term is the initial trion state $|i\rangle$. The difference is the recoil energy. The third term is the electron spin Zeeman energy that has no valley contribution. From these considerations, we can write the energy Zeeman shift for positive and negative magnetic field as measured in our experiment. For positive magnetic field we obtain

$$\Delta E_{\hbar\omega}^+ = E_Z - \left[\frac{1}{2}(\hbar\omega_c - \hbar\omega_T) + \frac{1}{2}g_e\mu_B B \right], \quad (11)$$

while for negative field

$$\Delta E_{\hbar\omega}^- = -E_Z - \left[\frac{1}{2}(\hbar\omega_c - \hbar\omega_T) - \frac{1}{2}g_e\mu_B B \right]. \quad (12)$$

The sum of the above Zeeman shifts for positive and negative field is

$$\Delta E_{\hbar\omega}^+ + \Delta E_{\hbar\omega}^- = -(\hbar\omega_c - \hbar\omega_T), \quad (13)$$

which is proportional to the difference between the cyclotron energy of an electron in a LL and the trion LL. This can be expressed as

$$\Delta E_{\hbar\omega}^+ + \Delta E_{\hbar\omega}^- = -\hbar e B \left(\frac{1}{m_3} - \frac{1}{m_T} \right), \quad (14)$$

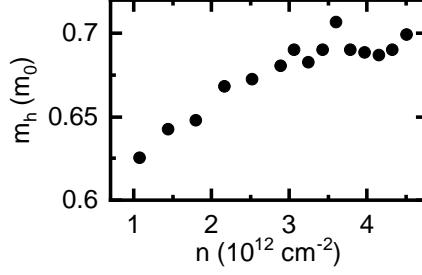
with $m_3 = 0.44m_0$ and $m_T = 2 \cdot 0.44m_0 + m_h m_0$. From our experiment we directly determine the Zeeman shift and corresponding g -factor of the negatively charged trion as a function of the carrier concentration. Hence, we can relate the measured g -factor for positive and negative magnetic field $g(s^+)$ and $g(s^-)$ to the energy difference of initial and final state of the trion, and therefore to the hole mass. We obtain

$$\frac{1}{2}g(s^+)\mu_B B + \frac{1}{2}g(s^-)\mu_B B = -\hbar e B \cdot \left(\frac{1}{m_3} - \frac{1}{m_T} \right), \quad (15)$$

which we can express as a function of the hole mass

$$m_h(n) = \left| \frac{-m_e(1 + m_e|g_{ave}(n)|)}{1/2 \cdot m_e|g_{ave}(n)| + 1} \right|, \quad (16)$$

with $|g_{ave}| = \frac{1}{2}(g(s^+) + g(s^-))$ and by using $\frac{\mu_B m_0}{\hbar e} \sim 0.5$.



SI Figure 7. Calculated energy shift from the carrier density difference of the LL with filling factor $\nu = +0$ and $\nu = +1$ taking into account the spin-orbit splitting of the conduction bands of $\Delta_{db} = 14 \text{ meV}$ [28] and the carrier density at which the Fermi level touches the upper spin-orbit split conduction bands.

VIII. QUANTIZED SPIN-VALLEY TEXTURE

The Zeeman shift of electrons in the spin-orbit split conduction band valleys in monolayer MoS₂ manifests from spin, the Berry phase and due to quantization of electrons in Landau levels in each valley. The shift for the lower conduction band c_1 is given by

$$E_{c_1} = \tau_s s_z 2\mu_B B + \tau_i m_e \mu_B B + \nu \frac{\hbar e B}{m_e}, \quad (17)$$

while the shift of the upper conduction band c_2 is

$$E_{c_2} = \Delta_{db} + \tau_s s_z 2\mu_B B + \tau_i m_e \mu_B B + \nu \frac{\hbar e B}{m_e}. \quad (18)$$

Here, the valley and spin indices are $\tau_s = \pm 1$ ($K = +1$ and $K' = -1$) and $\tau_i = \pm 1$ (+1 spin- \uparrow and -1 spin- \downarrow). Moreover, ν is the filling factor of the LL and Δ_{db} the energy splitting between c_1 and c_2 for no magnetic field applied. We model two LLs for each valley with $\nu = +0$ and $\nu = +1$ in K' . [30] After quantifying the energy shift of each LL of each spin in every valley, we can further calculate the density of states (DOS) as a function of the Fermi level E_F (applied gate voltage). From this quantity, we can then infer the number of electrons populating the spin- \downarrow and spin- \uparrow LLs to deduce the degree of spin polarization for a given E_F . We model each LL by using a Gaussian function

$$DOS_{LL} = \frac{e|B|}{h} \frac{1}{\sigma\sqrt{2\pi}} \exp\left[-\frac{(E - E_{LL})^2}{2\sigma^2}\right], \quad (19)$$

with eB/h as the degeneracy per unit area and the energetic position of the LL E_{LL} as defined in Eq. 17 and 18 and a FWHM of each LL of $\Gamma = 2\sqrt{2\ln(2)}\sigma = 4 \text{ meV}$ accounting for the experimentally observed inhomogeneous broadening in device A . The total DOS for all spin- \uparrow electrons is given through

$$DOS_{LL}^{\uparrow} = \sum_{i=0}^{\nu=1} DOS_{LL}^{\uparrow, K'} + \sum_{i=1}^{\nu=2} DOS_{LL}^{\uparrow, K} , \quad (20)$$

and the DOS for all spin- \downarrow electrons are given by

$$DOS_{LL}^{\downarrow} = \sum_{i=1}^{\nu=2} DOS_{LL}^{\downarrow, K} + \sum_{i=0}^{\nu=1} DOS_{LL}^{\downarrow, K'} . \quad (21)$$

By integrating the DOS to E_F we obtain the number of electrons populating each LL with the total number of electrons with spin- \uparrow

$$N_{\uparrow} = \int_0^{E_F} DOS_{LL}^{\uparrow} dE \quad (22)$$

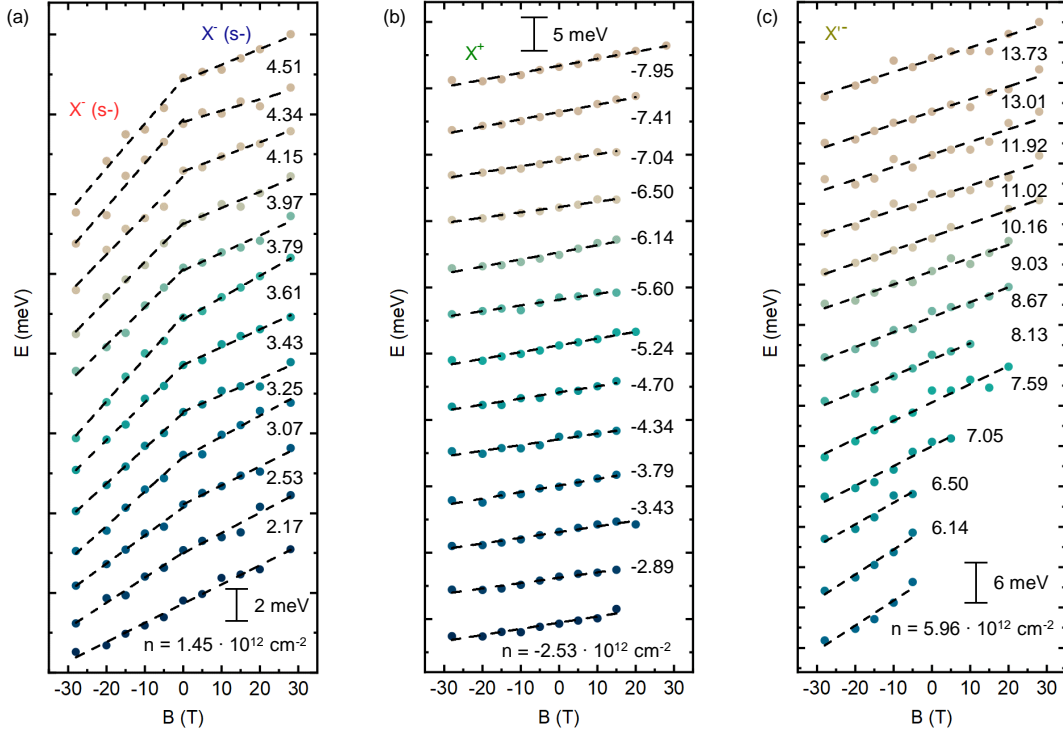
and spin- \downarrow

$$N_{\downarrow} = \int_0^{E_F} DOS_{LL}^{\downarrow} dE . \quad (23)$$

We can now compute the global degree of spin polarization all magnetic fields and E_F

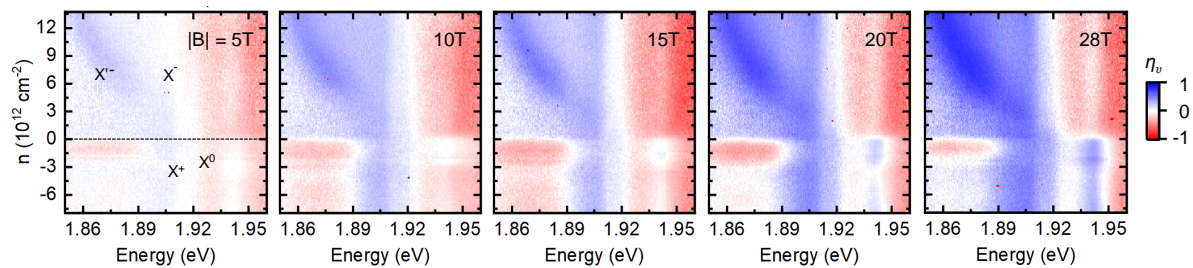
$$\eta_s(B, E_F) = \frac{N_{\downarrow} - N_{\uparrow}}{N_{\downarrow} + N_{\uparrow}} . \quad (24)$$

IX. VALLEY ZEEMAN SHIFT OF X^- , X^+ AND X'^-

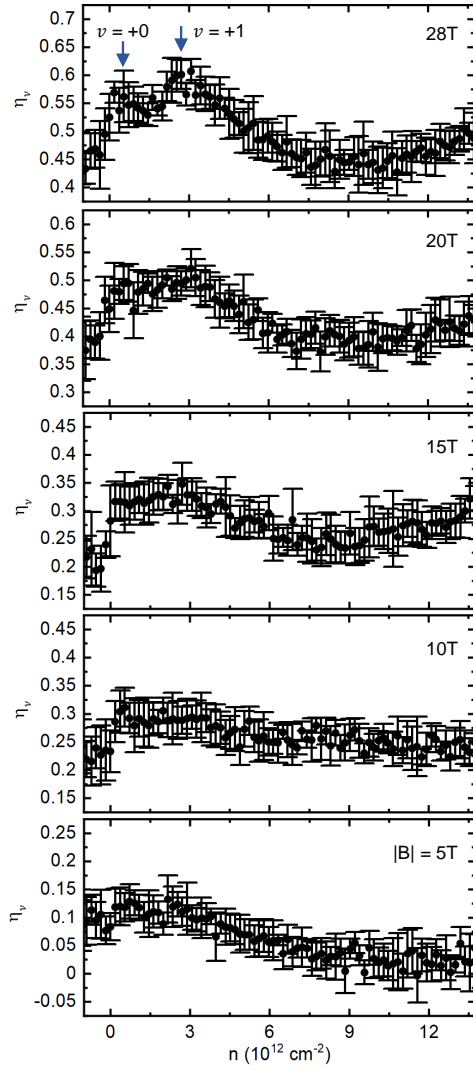


SI Figure 8. (a) Charge carrier dependent Zeeman shift of the negatively charged exciton X^- . The dashed lines are linear fits for positively and negatively fields, respectively. (b) Carrier density dependent Zeeman shift of the positively charged exciton X^+ . (c) Carrier density dependent Zeeman shift of the strongly dressed high density feature X'^- .

X. MAGNETIC FIELD AND DENSITY DEPENDENT VALLEY DICHROISM



SI Figure 9. False color maps of the energy and carrier density dependent degree of valley polarization η_v at $|B| = 5$ T, 10 T, 15 T, 20 T and 28 T. Charge neutrality is highlighted with the dashed black line. The X^- and X'^- reveal enhanced degree of polarization for higher magnetic field.



SI Figure 10. Electron density dependent degree of valley polarization of the *intravalley* trion X^- for magnetic fields ranging from $|B| = 5$ T to 28 T. For $|B| = 28$ T, LLs with filling factors of $\nu = +0$ and $\nu = +1$ are highlighted by the two arrows, respectively.

XI. MAGNETIC MOMENT OF BLOCH ELECTRONS: LATTICE HAMILTONIAN VS. ATOMIC CONTRIBUTIONS

The magnetic moment is comprised of a contribution due to the orbital motion of a Bloch electron and a contribution due to the electron spin. The z-component of the orbital magnetic moment is given by:

$$\mu_{z\mathbf{k}}^{\text{orb},n} = -\frac{e}{2m_e} \langle \Phi_{\mathbf{k}}^n | \hat{l}_z | \Phi_{\mathbf{k}}^n \rangle = -\frac{e}{2m_e} \langle \Phi_{\mathbf{k}}^n | \hat{x}\hat{p}_y - \hat{y}\hat{p}_x | \Phi_{\mathbf{k}}^n \rangle. \quad (25)$$

Consider the general expression $\langle \Phi_{\mathbf{k}}^n | \hat{x}_i \hat{p}_j | \Phi_{\mathbf{k}}^n \rangle$ and insert a complete set of Bloch states:

$$\langle \Phi_{\mathbf{k}}^n | \hat{x}_i \hat{p}_j | \Phi_{\mathbf{k}}^n \rangle = \sum_{n'\mathbf{k}'} \langle \Phi_{\mathbf{k}}^n | \hat{x}_i | \Phi_{\mathbf{k}'}^{n'} \rangle \langle \Phi_{\mathbf{k}'}^{n'} | \hat{p}_j | \Phi_{\mathbf{k}}^n \rangle. \quad (26)$$

The momentum matrix elements are diagonal in \mathbf{k} due to translational invariance:

$$\langle \Phi_{\mathbf{k}'}^{n'} | \hat{p}_j | \Phi_{\mathbf{k}}^n \rangle = \langle \Phi_{\mathbf{k}}^{n'} | \hat{p}_j | \Phi_{\mathbf{k}}^n \rangle \delta_{\mathbf{k},\mathbf{k}'}. \quad (27)$$

The position matrix element can be transformed using the Schrödinger equation of Bloch states,

$$H | \Phi_{\mathbf{k}}^n \rangle = \varepsilon_{\mathbf{k}}^n | \Phi_{\mathbf{k}}^n \rangle, \quad (28)$$

and the commutator relation [31]

$$\frac{1}{m_e} \hat{\mathbf{p}} = \frac{i}{\hbar} [H, \hat{\mathbf{r}}], \quad (29)$$

which holds in case of a local one-electron potential. It is still valid in the presence of spin-orbit interaction, as long as the latter can be approximately treated as an on-site potential.

Using Eqs. (27), (28) and (29), we find:

$$\langle \Phi_{\mathbf{k}}^n | \hat{x}_i \hat{p}_j | \Phi_{\mathbf{k}}^n \rangle = \sum_{n'} \frac{\hbar}{im_e} \langle \Phi_{\mathbf{k}}^n | \hat{p}_i | \Phi_{\mathbf{k}}^{n'} \rangle \frac{1}{\varepsilon_{\mathbf{k}}^n - \varepsilon_{\mathbf{k}}^{n'}} \langle \Phi_{\mathbf{k}}^{n'} | \hat{p}_j | \Phi_{\mathbf{k}}^n \rangle. \quad (30)$$

The crystal wave functions can be constructed as a linear combination of localized orbitals in the following way such that they fulfill Bloch's theorem:

$$| \Phi_{\mathbf{k}}^n \rangle = \sum_{\alpha} c_{\alpha}^n(\mathbf{k}) | \mathbf{k}\alpha \rangle, \quad | \mathbf{k}\alpha \rangle = \frac{1}{\sqrt{N}} \sum_{\mathbf{R}} e^{i\mathbf{k}\cdot\mathbf{R}} | \mathbf{R}\alpha \rangle \quad (31)$$

with the orthonormality relations

$$\langle \mathbf{R}\alpha | \mathbf{R}'\alpha' \rangle = \delta_{\mathbf{R}\mathbf{R}'} \delta_{\alpha\alpha'} \quad (32)$$

and

$$\langle \mathbf{k}\alpha | \mathbf{k}'\alpha' \rangle = \delta_{\mathbf{k}\mathbf{k}'} \delta_{\alpha\alpha'}, \quad (33)$$

where N is the number of lattice sites. We can formulate the crystal (lattice) Hamiltonian in terms of the localized orbitals:

$$H = \sum_{\mathbf{R}\mathbf{R}'\alpha\alpha'} t_{\mathbf{R}\mathbf{R}'}^{\alpha\alpha'} |\mathbf{R}\alpha\rangle \langle \mathbf{R}'\alpha'|. \quad (34)$$

Inserting the ansatz (31) into Eq. (30), we obtain:

$$\langle \Phi_{\mathbf{k}}^n | \hat{x}_i \hat{p}_j | \Phi_{\mathbf{k}}^n \rangle = \sum_{n'} \frac{\hbar}{im_e} \frac{1}{\varepsilon_{\mathbf{k}}^n - \varepsilon_{\mathbf{k}}^{n'}} \sum_{\alpha\alpha'} (c_{\alpha}^n(\mathbf{k}))^* c_{\alpha'}^{n'}(\mathbf{k}) \langle \mathbf{k}\alpha | \hat{p}_i | \mathbf{k}\alpha' \rangle \sum_{\alpha\alpha'} (c_{\alpha'}^{n'}(\mathbf{k}))^* c_{\alpha}^n(\mathbf{k}) \langle \mathbf{k}\alpha' | \hat{p}_j | \mathbf{k}\alpha \rangle. \quad (35)$$

Following [32], we analyze the momentum matrix element by using the commutator relation (29) again, transforming the momentum states according to (31) and inserting a complete set of position states:

$$\langle \mathbf{k}\alpha' | \hat{p}_j | \mathbf{k}\alpha \rangle = -\frac{im_e}{\hbar} \frac{1}{N} \sum_{\mathbf{R}, \mathbf{R}'} e^{i\mathbf{k}\cdot(\mathbf{R}-\mathbf{R}')} \int d\mathbf{r} [\langle \mathbf{R}'\alpha' | \hat{r}_j | \mathbf{r} \rangle \langle \mathbf{r} | H | \mathbf{R}\alpha \rangle - \langle \mathbf{R}'\alpha' | H | \mathbf{r} \rangle \langle \mathbf{r} | \hat{r}_j | \mathbf{R}\alpha \rangle]. \quad (36)$$

One has to distinguish between the continuous space variable \mathbf{r} and the discrete unit-cell label \mathbf{R} . The position operator acts as $\hat{r}_j | \mathbf{r} \rangle = r_j | \mathbf{r} \rangle$. The momentum matrix element contains contributions that can be directly related to the discrete lattice as well as contributions that arise due to the spatial extension of orbitals. We separate these contributions by shifting $\mathbf{r} \rightarrow \mathbf{r} + \mathbf{R}'$ in the first term and $\mathbf{r} \rightarrow \mathbf{r} + \mathbf{R}$ in the second term:

$$\begin{aligned} \langle \mathbf{k}\alpha' | \hat{p}_j | \mathbf{k}\alpha \rangle &= -\frac{im_e}{\hbar} \frac{1}{N} \sum_{\mathbf{R}, \mathbf{R}'} e^{i\mathbf{k}\cdot(\mathbf{R}-\mathbf{R}')} \int d\mathbf{r} \\ &\quad [\langle \mathbf{R}'\alpha' | r_j + R'_j | \mathbf{r} + \mathbf{R}' \rangle \langle \mathbf{r} + \mathbf{R}' | H | \mathbf{R}\alpha \rangle \\ &\quad - \langle \mathbf{R}'\alpha' | H | \mathbf{r} + \mathbf{R} \rangle \langle \mathbf{r} + \mathbf{R} | r_j + R_j | \mathbf{R}\alpha \rangle] \\ &= -\frac{im_e}{\hbar} \frac{1}{N} \sum_{\mathbf{R}, \mathbf{R}'} e^{i\mathbf{k}\cdot(\mathbf{R}-\mathbf{R}')} (R'_j - R_j) \langle \mathbf{R}'\alpha' | H | \mathbf{R}\alpha \rangle \\ &\quad - \frac{im_e}{\hbar} \frac{1}{N} \sum_{\mathbf{R}, \mathbf{R}'} e^{i\mathbf{k}\cdot(\mathbf{R}-\mathbf{R}')} \int d\mathbf{r} r_j \\ &\quad [\langle \mathbf{R}'\alpha' | \mathbf{r} + \mathbf{R}' \rangle \langle \mathbf{r} + \mathbf{R}' | H | \mathbf{R}\alpha \rangle \\ &\quad - \langle \mathbf{R}'\alpha' | H | \mathbf{r} + \mathbf{R} \rangle \langle \mathbf{r} + \mathbf{R} | \mathbf{R}\alpha \rangle], \end{aligned} \quad (37)$$

where we made use of the completeness of position states again to derive the first term of the second line. This so-called Peierls contribution given by *inter*-site hopping can be written as a generalized Fermi velocity:

$$\begin{aligned}
& -\frac{im_e}{\hbar} \frac{1}{N} \sum_{\mathbf{R}, \mathbf{R}'} e^{i\mathbf{k} \cdot (\mathbf{R} - \mathbf{R}')} (R'_j - R_j) \langle \mathbf{R}' \alpha' | H | \mathbf{R} \alpha \rangle \\
& = \frac{m_e}{\hbar} \frac{\partial}{\partial k_j} \frac{1}{N} \sum_{\mathbf{R}, \mathbf{R}'} e^{i\mathbf{k} \cdot (\mathbf{R} - \mathbf{R}')} \langle \mathbf{R}' \alpha' | H | \mathbf{R} \alpha \rangle \\
& = \frac{m_e}{\hbar} \frac{\partial}{\partial k_j} \tilde{H}_{\mathbf{k}}^{\alpha' \alpha}.
\end{aligned} \tag{38}$$

It follows from the Schrödinger equation (28) that the Hamiltonian $\tilde{H}_{\mathbf{k}}^{\alpha \alpha'}$ defines the tight-binding-like eigenvalue problem

$$\sum_{\alpha'} \tilde{H}_{\mathbf{k}}^{\alpha \alpha'} c_{\alpha'}^n(\mathbf{k}) = \varepsilon_{\mathbf{k}}^n c_{\alpha}^n(\mathbf{k}). \tag{39}$$

The second term in Eq. (37) contains continuum contributions due to the finite extension of the electron wave functions. It can be written as

$$\begin{aligned}
& -\frac{im_e}{\hbar} \frac{1}{N} \sum_{\mathbf{R}, \mathbf{R}'} e^{i\mathbf{k} \cdot (\mathbf{R} - \mathbf{R}')} \int d\mathbf{r} r_j \sum_{\mathbf{R}'', \alpha''} [\langle \mathbf{R}' \alpha' | \mathbf{r} + \mathbf{R}' \rangle \langle \mathbf{r} + \mathbf{R}' | \mathbf{R}'' \alpha'' \rangle \langle \mathbf{R}'' \alpha'' | H | \mathbf{R} \alpha \rangle \\
& \quad - \langle \mathbf{R}' \alpha' | H | \mathbf{R}'' \alpha'' \rangle \langle \mathbf{R}'' \alpha'' | \mathbf{r} + \mathbf{R} \rangle \langle \mathbf{r} + \mathbf{R} | \mathbf{R} \alpha \rangle] \\
& = -\frac{im_e}{\hbar} \frac{1}{N} \sum_{\mathbf{R}, \mathbf{R}'} e^{i\mathbf{k} \cdot (\mathbf{R} - \mathbf{R}')} \int d\mathbf{r} r_j \sum_{\mathbf{R}'', \alpha''} [(\chi_{\mathbf{R}' \alpha'}(\mathbf{r} + \mathbf{R}'))^* \chi_{\mathbf{R}'' \alpha''}(\mathbf{r} + \mathbf{R}') \langle \mathbf{R}'' \alpha'' | H | \mathbf{R} \alpha \rangle \\
& \quad - \langle \mathbf{R}' \alpha' | H | \mathbf{R}'' \alpha'' \rangle (\chi_{\mathbf{R}'' \alpha''}(\mathbf{r} + \mathbf{R}))^* \chi_{\mathbf{R} \alpha}(\mathbf{r} + \mathbf{R})]
\end{aligned} \tag{40}$$

with the wave functions $\chi_{\mathbf{R} \alpha}(\mathbf{r}) = \langle \mathbf{r} | \mathbf{R} \alpha \rangle$. This term accounts on the one hand for all atomic or *intra*-site ($\mathbf{R} = \mathbf{R}'$) processes and on the other hand for corrections to the *inter*-site processes contained in the Peierls term. Hence, we can split the momentum matrix element into three contributions:

$$\langle \mathbf{k} \alpha' | \hat{p}_j | \mathbf{k} \alpha \rangle = \frac{m_e}{\hbar} \frac{\partial}{\partial k_j} \tilde{H}_{\mathbf{k}}^{\alpha' \alpha} + p_{\mathbf{k}, j}^{\alpha' \alpha} |_{\text{inter-site corr.}} + p_{\mathbf{k}, j}^{\alpha' \alpha} |_{\text{intra-site corr.}}. \tag{41}$$

In the limit of well-localized orbitals, the dominant correction is given by the *intra*-site term [32]. It is obtained by using the lattice periodicity, $\chi_{\mathbf{R} \alpha}(\mathbf{r} + \mathbf{R}) = \chi_{\mathbf{0} \alpha}(\mathbf{r})$, to shift the origins of all wave functions to the same unit cell, which is labeled $\mathbf{0}$. We then identify those terms

where the wave function arguments also lie within the same unit cell ($\mathbf{R}'' = \mathbf{R}'$ in the first term, $\mathbf{R}'' = \mathbf{R}$ in the second term):

$$\begin{aligned}
p_{\mathbf{k},j}^{\alpha'\alpha} \Big|_{\text{intra-site corr.}} &= -\frac{im_e}{\hbar} \frac{1}{N} \sum_{\mathbf{R},\mathbf{R}'} e^{i\mathbf{k}\cdot(\mathbf{R}-\mathbf{R}')} \int d\mathbf{r} r_j \sum_{\alpha''} \\
& \left[(\chi_{0\alpha'}(\mathbf{r}))^* \chi_{0\alpha''}(\mathbf{r}) \langle \mathbf{R}'\alpha'' | H | \mathbf{R}\alpha \rangle - \langle \mathbf{R}'\alpha' | H | \mathbf{R}\alpha'' \rangle (\chi_{0\alpha''}(\mathbf{r}))^* \chi_{0\alpha}(\mathbf{r}) \right] \\
&= -\frac{im_e}{\hbar} \int d\mathbf{r} r_j \sum_{\alpha''} \left((\chi_{0\alpha'}(\mathbf{r}))^* \chi_{0\alpha''}(\mathbf{r}) \tilde{H}_{\mathbf{k}}^{\alpha''\alpha} - \tilde{H}_{\mathbf{k}}^{\alpha'\alpha''} (\chi_{0\alpha''}(\mathbf{r}))^* \chi_{0\alpha}(\mathbf{r}) \right) \\
&= -\frac{im_e}{\hbar} \sum_{\alpha''} \left(r_j^{\alpha'\alpha''} \tilde{H}_{\mathbf{k}}^{\alpha''\alpha} - \tilde{H}_{\mathbf{k}}^{\alpha'\alpha''} r_j^{\alpha''\alpha} \right)
\end{aligned} \tag{42}$$

with the atom-like dipole matrix elements

$$r_j^{\alpha\alpha'} = \int d\mathbf{r} r_j (\chi_{0\alpha}(\mathbf{r}))^* \chi_{0\alpha'}(\mathbf{r}) \tag{43}$$

forcing the usual optical selection rules $\Delta l = \pm 1, \Delta m = 0, \pm 1$. Note that the *intra*-site term (42) needs to take into account the same set of localized orbitals that is used to set up the lattice Hamiltonian (34). The fact that the coupling to the magnetic field via the vector potential has to be two-fold in a tight-binding or lattice approach has also been discussed in Ref. [33]. There are always contributions that can not be captured by the so-called Peierls substitution [32] in the lattice Hamiltonian leading to the first term in (41). If we nevertheless use the Peierls contribution alone, we end up with the following lattice formulation of the orbital magnetic moment:

$$\begin{aligned}
\mu_{z\mathbf{k}}^{\text{orb},n} \Big|_{\text{lat}} &= -\frac{e}{2m_e} \frac{\hbar}{im_e} \left(\frac{m_e}{\hbar} \right)^2 \sum_{n'} \frac{1}{\varepsilon_{\mathbf{k}}^n - \varepsilon_{\mathbf{k}}^{n'}} \sum_{\alpha\alpha'} (c_{\alpha}^n(\mathbf{k}))^* c_{\alpha'}^{n'}(\mathbf{k}) \frac{\partial}{\partial k_x} \tilde{H}_{\mathbf{k}}^{\alpha\alpha'} \sum_{\alpha\alpha'} (c_{\alpha'}^{n'}(\mathbf{k}))^* c_{\alpha}^n(\mathbf{k}) \frac{\partial}{\partial k_y} \tilde{H}_{\mathbf{k}}^{\alpha'\alpha} \\
&\quad - (x \leftrightarrow y) \\
&= \frac{ie}{2\hbar} \sum_{n'} \frac{1}{\varepsilon_{\mathbf{k}}^n - \varepsilon_{\mathbf{k}}^{n'}} \left\{ \sum_{\alpha\alpha'} (c_{\alpha}^n(\mathbf{k}))^* c_{\alpha'}^{n'}(\mathbf{k}) \frac{\partial}{\partial k_x} \tilde{H}_{\mathbf{k}}^{\alpha\alpha'} \sum_{\alpha\alpha'} (c_{\alpha'}^{n'}(\mathbf{k}))^* c_{\alpha}^n(\mathbf{k}) \frac{\partial}{\partial k_y} \tilde{H}_{\mathbf{k}}^{\alpha'\alpha} - c.c. \right\} \\
&= -\frac{e}{\hbar} \sum_{n'} \frac{1}{\varepsilon_{\mathbf{k}}^n - \varepsilon_{\mathbf{k}}^{n'}} \text{Im} \left\{ \sum_{\alpha\alpha'} (c_{\alpha}^n(\mathbf{k}))^* c_{\alpha'}^{n'}(\mathbf{k}) \frac{\partial}{\partial k_x} \tilde{H}_{\mathbf{k}}^{\alpha\alpha'} \sum_{\alpha\alpha'} (c_{\alpha'}^{n'}(\mathbf{k}))^* c_{\alpha}^n(\mathbf{k}) \frac{\partial}{\partial k_y} \tilde{H}_{\mathbf{k}}^{\alpha'\alpha} \right\}.
\end{aligned} \tag{44}$$

In a simple two-band model, the structure of this expression leads to equal orbital magnetic moments for conduction and valence electrons. Corrections are expected due to transitions from each band, respectively, to energetically higher and lower bands. Moreover, if the two

fundamental bands are composed of localized orbitals that do not allow for atom-like dipole transitions (e.g. d_{z^2} - and $d_{x^2-y^2}/d_{xy}$ -orbitals in transition metal dichalcogenide monolayers), the *intra*-site correction will vanish. The exciton g-factor, calculated directly from the magnetic moments of conduction and valence bands at the \mathbf{K} -point as $g_X = 2(\mu_{z\mathbf{K}}^c - \mu_{z\mathbf{K}}^v)/\mu_B$, will therefore be zero since the net spin of the exciton is zero. This is consistent with the $k \cdot p$ -picture discussed in Ref. [33].

-
- [1] A. Castellanos-Gomez, M. Buscema, R. Molenaar, V. Singh, L. Janssen, H. S. J. van der Zant, and G. A. Steele, *2D Materials* **1**, 011002 (2014), URL <https://doi.org/10.1088/2053-1583/1/1/011002>.
- [2] J. Wierzbowski, J. Klein, F. Sigger, C. Straubinger, M. Kremser, T. Taniguchi, K. Watanabe, U. Wurstbauer, A. W. Holleitner, M. Kaniber, et al., *Scientific Reports* **7** (2017), URL <https://doi.org/10.1038/s41598-017-09739-4>.
- [3] C. R. Dean, A. F. Young, I. Meric, C. Lee, L. Wang, S. Sorgenfrei, K. Watanabe, T. Taniguchi, P. Kim, K. L. Shepard, et al., *Nature Nanotechnology* **5**, 722 (2010), URL <https://doi.org/10.1038/nnano.2010.172>.
- [4] C. Robert, M. A. Semina, F. Cadiz, M. Manca, E. Courtade, T. Taniguchi, K. Watanabe, H. Cai, S. Tongay, B. Lassagne, et al., *Physical Review Materials* **2** (2018), URL <https://doi.org/10.1103/physrevmaterials.2.011001>.
- [5] J. G. Roch, G. Froehlicher, N. Leisgang, P. Makk, K. Watanabe, T. Taniguchi, and R. J. Warburton, *Nature Nanotechnology* **14**, 432 (2019), URL <https://doi.org/10.1038/s41565-019-0397-y>.
- [6] K. K. Kim, A. Hsu, X. Jia, S. M. Kim, Y. Shi, M. Dresselhaus, T. Palacios, and J. Kong, *ACS Nano* **6**, 8583 (2012), URL <https://doi.org/10.1021/nm301675f>.
- [7] B. Hunt, J. D. Sanchez-Yamagishi, A. F. Young, M. Yankowitz, B. J. LeRoy, K. Watanabe, T. Taniguchi, P. Moon, M. Koshino, P. Jarillo-Herrero, et al., *Science* **340**, 1427 (2013), URL <https://doi.org/10.1126/science.1237240>.
- [8] A. Laturia, M. L. V. de Put, and W. G. Vandenberghe, *npj 2D Materials and Applications* **2** (2018), URL <https://doi.org/10.1038/s41699-018-0050-x>.
- [9] X. Cui, G.-H. Lee, Y. D. Kim, G. Arefe, P. Y. Huang, C.-H. Lee, D. A. Chenet, X. Zhang, L. Wang, F. Ye, et al., *Nature Nanotechnology* **10**, 534 (2015), URL <https://doi.org/10.1038/nnano.2015.70>.
- [10] A. Allain, J. Kang, K. Banerjee, and A. Kis, *Nature Materials* **14**, 1195 (2015), URL <https://doi.org/10.1038/nmat4452>.
- [11] M. Rohlfing and S. G. Louie, *Physical Review B* **62**, 4927 (2000), URL <https://link.aps.org/doi/10.1103/PhysRevB.62.4927>.

- [12] L. J. Sham and T. M. Rice, *Physical Review* **144**, 708–714 (1966), URL <https://link.aps.org/doi/10.1103/PhysRev.144.708>.
- [13] M. M. Denisov and V. P. Makarov, *physica status solidi (b)* **56**, 9–59 (1973), ISSN 1521-3951.
- [14] D. Y. Qiu, T. Cao, and S. G. Louie, *Physical Review Letters* **115** (2015), URL <https://doi.org/10.1103/physrevlett.115.176801>.
- [15] A. Esser, R. Zimmermann, and E. Runge, *physica status solidi (b)* **227**, 317 (2001), ISSN 1521-3951, URL [http://onlinelibrary.wiley.com/doi/10.1002/1521-3951\(200110\)227:2<317::AID-PSSB317>3.0.CO;2-S/abstract](http://onlinelibrary.wiley.com/doi/10.1002/1521-3951(200110)227:2<317::AID-PSSB317>3.0.CO;2-S/abstract).
- [16] M. Florian, M. Hartmann, A. Steinhoff, J. Klein, A. W. Holleitner, J. J. Finley, T. O. Wehling, M. Kaniber, and C. Gies, *Nano Letters* **18**, 2725 (2018), URL <https://doi.org/10.1021/acs.nanolett.8b00840>.
- [17] A. Steinhoff, M. Rösner, F. Jahnke, T. O. Wehling, and C. Gies, *Nano Letters* **14**, 3743 (2014), URL <https://doi.org/10.1021/nl500595u>.
- [18] G.-B. Liu, W.-Y. Shan, Y. Yao, W. Yao, and D. Xiao, *Physical Review B* **88** (2013), URL <https://doi.org/10.1103/physrevb.88.085433>.
- [19] M. Rösner, E. Şaşıoğlu, C. Friedrich, S. Blügel, and T. O. Wehling, *Physical Review B* **92**, 085102 (2015), URL <https://link.aps.org/doi/10.1103/PhysRevB.92.085102>.
- [20] H. Yu, G.-B. Liu, P. Gong, X. Xu, and W. Yao, *Nature Communications* **5** (2014), URL <https://doi.org/10.1038/ncomms4876>.
- [21] A. Steinhoff, M. Florian, A. Singh, K. Tran, M. Kolarczik, S. Helmrich, A. W. Achtstein, U. Woggon, N. Owschimikow, F. Jahnke, et al., *Nature Physics* **14**, 1199 (2018), ISSN 1745-2481, URL <https://www.nature.com/articles/s41567-018-0282-x>.
- [22] S. Balay, S. Abhyankar, M. Adams, J. Brown, P. Brune, K. Buschelman, L. Dalcin, V. Eijkhout, W. Gropp, D. Kaushik, et al., *PETSc Web page*, <http://www.mcs.anl.gov/petsc/> (2016), URL <http://www.mcs.anl.gov/petsc/>.
- [23] E. Courtade, M. Semina, M. Manca, M. M. Glazov, C. Robert, F. Cadiz, G. Wang, T. Taniguchi, K. Watanabe, M. Pierre, et al., *Physical Review B* **96** (2017), URL <https://doi.org/10.1103/physrevb.96.085302>.
- [24] R. Pisoni, A. Kormányos, M. Brooks, Z. Lei, P. Back, M. Eich, H. Overweg, Y. Lee, P. Rickhaus, K. Watanabe, et al., *Physical Review Letters* **121** (2018), URL <https://doi.org/10.1103/physrevlett.121.247701>.

- [25] E. Liu, J. van Baren, T. Taniguchi, K. Watanabe, Y.-C. Chang, and C. H. Lui, Physical Review Letters **124** (2020), URL <https://doi.org/10.1103/physrevlett.124.097401>.
- [26] A. Stier, N. Wilson, K. Velizhanin, J. Kono, X. Xu, and S. Crooker, Physical Review Letters **120** (2018), URL <https://doi.org/10.1103/physrevlett.120.057405>.
- [27] J. Jadczak, J. Kutrowska-Girzycka, M. Bieniek, T. Kazimierczuk, P. Kossacki, K. Watanabe, T. Taniguchi, C.-H. Ho, A. Wójs, P. Hawrylak, et al., arXiv preprint arXiv:2001.07929 (2020).
- [28] C. Robert, B. Han, P. Kapuscinski, A. Delhomme, C. Faugeras, T. Amand, M. R. Molas, M. Bartos, K. Watanabe, T. Taniguchi, et al., arXiv preprint arXiv:2002.03877 (2020).
- [29] T. P. Lyons, S. Dufferwiel, M. Brooks, F. Withers, T. Taniguchi, K. Watanabe, K. S. Novoselov, G. Burkard, and A. I. Tartakovskii, Nature Communications **10** (2019), URL <https://doi.org/10.1038/s41467-019-10228-7>.
- [30] F. Rose, M. O. Goerbig, and F. Piéchon, Physical Review B **88** (2013), URL <https://doi.org/10.1103/physrevb.88.125438>.
- [31] M. Gajdoš, K. Hummer, G. Kresse, J. Furthmüller, and F. Bechstedt, Physical Review B **73** (2006), URL <https://doi.org/10.1103/physrevb.73.045112>.
- [32] J. M. Tomczak and S. Biermann, Physical Review B **80** (2009), URL <https://doi.org/10.1103/physrevb.80.085117>.
- [33] G. Wang, L. Bouet, M. M. Glazov, T. Amand, E. L. Ivchenko, E. Palleau, X. Marie, and B. Urbaszek, 2D Materials **2**, 034002 (2015), URL <https://doi.org/10.1088/2053-1583/2/3/034002>.